Volume 1·Issue 1·January 2022 ISSN 2754-5652(Online)

SCIENTIFIC
Publishing Limited

New Energy Exploitation and Application

Volume 1 Issue 1 • January 2022

New Energy Exploitation and Application

Editor-in-Chief

Adnan SÖZEN

SCIENTIFIC Publishing Limited

Volume 1 | Issue 1 | January 2022 | Page1-36

New Energy Exploitation and Application

Contents

Research Articles

Review Article

Case

SCIENTIFIC Publishing Limited

New Energy Exploitation and Application

http://ojs.ukscip.com/index.php/NEEA/issue/view/2

REVIEW ARTICLE

Geoinformation Systems in the Development of Solar Energy in Turkmenistan

A.M.Penjiyev[*]

Turkmen State Institute of Architecture and Civil Engineering, 744032, Turkmenistan

Received: 22 December 2021; **Accepted:** 20 January 2022; **Published Online:** 25 January 2022

Abstract: The article considers the scientifically substantiated, systematized solar energy resource potentials of Turkmenistan. Geoinformation technological maps based on solar energy resource potentials for use in Turkmenistan have been developed, compiled. The obtained technical, economic potentials and environmental indicators from the use of power plants based on them have been developed. Solar geoinformation technological maps for the placement of water-lifting plants and solar thermal cells make it possible to increase energy efficiency and environmental safety. The expected environmental and economic effect of the use of solar-energy technological installations in the conditions of the Karakum desert zone is from: reduction of various harmful substances into the environment when selling at a price of 6 US dollars to CO_2 carbon fund - 425437.3 tons per year, financial profit will be $ 2.5 million; fossil fuel savings 82.160 thousand tons of fuel equivalent per year or electricity generation of 663.4 GWh per year.

Keywords: Geographic information systems, Maps, Solar energy, Installations, Technologies, Energy supply, Energy efficiency, Karakum desert, Turkmenistan

1. Introduction

The urgency of the problem. Turkmenistan actively implements a policy of positive neutrality in the system of international relations and supports the solution of world energy, economic and environmental problems.

At the inauguration of Gurbanguly Berdimuhamedov for the post of President of Turkmenistan (2017), it was emphasized that the country will provide great support for the efficient use of renewable energy sources (RES). A fundamentally new integrated approach is environmental policy, the issues of the UN Convention on Climate Change, to combat desertification and the development of deserts [1-3,5].

To achieve the main goal of the energy strategy of Turkmenistan, it is necessary to solve a number of interrelated tasks, including: ensuring energy security and interaction of the fuel and energy sector with the country's economy in the interests of the population; increasing energy efficiency by optimizing the capacity of power generating structures, introducing innovative energy

*Corresponding Author:
A.M.Penjiyev,
Turkmen State Institute of Architecture and Civil Engineering, 744032, Turkmenistan;
Email: ampenjiev@rambler.ru

DOI: https://doi.org/10.54963/neea.v1i1.11

saving technologies; economic assessment, assistance in the development of the country's resource base; support of the scientific, technical and organizational potential of the fuel and energy complex; increasing the economic efficiency of innovative transformations in the spheres of production, transmission of energy and the use of the formation of mechanisms of state regulation, the functioning of the energy sector [3].

The territory of Turkmenistan is 80% occupied by the Karakum Desert, and a significant number of people live in the zone of decentralized energy supply, therefore, the development of technology and the use of renewable energy resources is an urgent problem. RES resources in terms of volume can cover a significant part of the consumption of fuel and energy resources and solve urgent energy, economic, environmental and social problems in Turkmenistan [3-5].

A lot of work has been done in Turkmenistan on the use of renewable energy sources, in particular, in solar energy, significant scientific results have been achieved. At the same time, there is a lack of foundations for a scientific generalizing, systematic analysis of energy potentials. The regions of Turkmenistan that have significant renewable energy resources for the use of energy efficient technologies and installations based on renewable energy sources have not been identified, recommendations have not been formulated for the implementation of developments, development and development of renewable energy energy potentials, taking into account innovative techniques. Geoinformation technological maps and nomograms were not compiled for a feasibility study (FS) [7,8].

Geographic information system or geographic information systems (GIS) is a new direction, which is used as a tool for technological solutions that allows you to search for additional information, analyze in this case a digital technological map of the area, taking into account scientific and engineering knowledge, technical, energy, economic, environmental potentials for use RES [8].

The results of scientific research will fill this gap and will contribute to the large-scale development of renewable energy, saving energy resources, improving the socio-economic and living conditions of pastures, reducing the anthropogenic load on the environment and climate change. On the basis of a literature review, scientific research on the use of renewable energy sources in Turkmenistan, the goals and objectives of research work have been determined.

Purpose of work

Scientifically substantiate, systematize, calculate and study solar energy potentials for the development, creation, implementation and use of energy technologies based on renewable energy sources for sustainable development of Turkmenistan.

Research methodology

Based on a systematic approach to the object of research as an integral complex of theoretical, practical and experimental works using energy technologies based on renewable energy sources for sustainable development of Turkmenistan. The subject of research is the energy efficiency of complex renewable energy technologies for the use of water supply and the development of the Karakum desert. The methodological base of the research was formed by the developed mathematical models, theoretical obtained empirical formulas, created geoinformation technological maps, proposed developments, experimentally implemented power plants based on renewable energy sources in various industries of Turkmenistan.

2. Geoinformation Technologies in the Development of Renewable Energy

The development of renewable energy (RE) currently requires solving not only technological problems, the adoption of legislative acts, the provision of state financial support for projects, but also substantiation of issues related to the analysis of energy resource potentials of various types of renewable energy sources (RES).

Renewable energy sources include energy sources of solar origin: solar radiation, wind, hydraulic energy of rivers, biomass, seas and oceans), non-solar energy (geothermal energy, energy of tides), various waste and low-potential heat sources.

The types of renewable energy sources are wide and heterogeneous in the presented scientific article, energy resource potentials (technical, economic, environmental) compiled by geoinformation maps of solar energy on the territory of Turkmenistan are considered [3-8].

Vast geographic datasets have been accumulated that provide the actual basis for RES for the use of renewable energy technologies in various forms. Moreover, in addition to the problem of verifying these data, analyzing the adequacy of methods for obtaining them, there are difficulties in their visual display in a form convenient for analysis. An important task is to accumulate them in the form of databases, as well as to map the potential of solar energy for use in various regions of the country.

In addition to the scientific and methodological significance, such studies are of great practical relevance, since databases of geographic information systems (GIS) should become an important tool for analyzing the energy efficiency of the practical use of solar energy in various regions of Turkmenistan, in particular the Karakum desert and drawing up a feasibility study in the preparation of design estimate documentation and management decisions of use, taking into account technological and economic indicators [6-8].

3. Scientific Research of the Development of Creating a GIS Technological Map

In the course of scientific theoretical and experimental research, solar energy technologies and installations have been studied. The bases of the use of solar energy potentials on the territory of Turkmenistan have been scientifically substantiated and theoretically systematized. A geoinformation solar energy map has been developed, see Figure 1.

On the basis of a GIS map, the energy characteristics of a solar greenhouse, photovoltaic modules under uneven illumination, solar installations with axisymmetric concentrators have been investigated, a geoinformation technological map has been developed for placing solar water-lifting installations in the Karakum desert.

The theoretical, experimental calculated results are systematized according to a formalized method, resource potentials and the volume of reduction of anthropogenic loads on the environment from the use of solar power plants when converted into thermal and electrical energy are determined. The calculations took into account the natural and climatic conditions: the astronomical duration of the sunshine during the month; average annual and monthly operating temperature of the solar installation and the environment; the fraction of scattered radiation, surface albedo, angular parameters of the arrival of solar energy on an inclined and normally oriented surface during a month; hour angle of movement of solar declination and inclination of the surface to the horizon; specific energy parameters of a solar installation. Until now, such calculations with the assessment of technical, economic, potentials and environmental indicators have not been carried out in Turkmenistan. The results are shown in Table 1 [8].

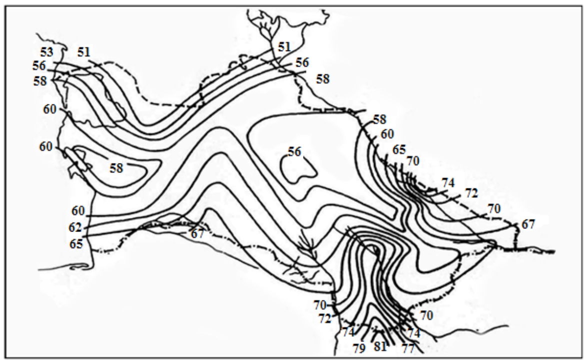

Figure 1. Geographic information map of the solar-energy balance in the territory of Turkmenistan (Wt h /cm^{2}year)

The distribution of the gross and technical potentials of solar energy during conversion into thermal energy and electricity in the Central Karakum by months (kWh /m^2 per month) has been calculated; the histogram is shown in Figure 2.

Table 1. The energy resource potentials of solar energy from conversion into thermal and electric energy from 1 sq. meters by regions of Turkmenistan

Resources gross, (kWh / m^{2}year)	Potentials		Anthropogenic load of harmful substances, (kg / m^{2}year)					
	Technical, (kWh / m^{2}year)	Fuel economy (kg c.f. m^2 / year)	SO_2	NO_x	CO	CH_4	CO_2	Solids
Northern region								
1757,4	1227,59*	490,90	10,20	5,49	0,71	1,50	784,96	1,07
	244,84**	97,94	2,035	1,09	0,14	0,31	156,62	0,21
	Southeast region							
1895,9	1296,78*	518,74	10,78	5,80	0,75	1,59	829,49	1,13
	248,55**	99,44	2,07	1,11	0,14	0,30	158,98	0,22
Region Central Karakum								
1844,6	1256,44*	502,61	10,44	5,62	0,72	1,54	803,68	1,09
	242,44**	96,98	2,01	1,08	0,14	0,31	155,08	0,21
South region								
1725,6	1234,46*	493,81	10,26	5,52	0,71	1,51	789,62	1,10
	225,29**	90,14	1,87	1,01	0,13	0,28	144,11	0,20
West region								
1685,4	1177,12*	470,88	9,78	5,26	0,68	1,44	752,9	1,02
	222,60**	89,06	1,85	0,99	0,13	0,27	142,4	0,20

Note: in the line * conversion to heat energy; ** - electricity.

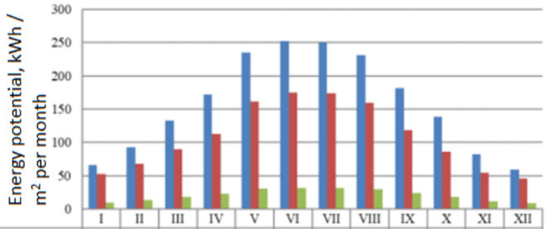

	I	II	III	IV	V	VI	VII	VIII	IX	X	XI	XII
Ei - gross	66,3	93,1	132,7	172,2	235,1	252,6	250,2	231,6	181,6	138,5	82,6	59,4
Wtt/St - heat	52,753	67,76	90,19	112,3	161,43	174,4	174,12	159,6	118,14	85,706	54,235	46,154
Wtf/Sf - electricity	9,4006	13,041	18,161	22,841	30,353	32,022	31,496	29,384	23,579	18,523	11,39	8,3638

Figure 2. Distribution of gross and technical potentials of solar energy from conversion to thermal energy and electricity in the Central Karakum Desert by months per 1 square meter

Development, creation and research of the energy characteristics of a solar greenhouse for growing tropical and subtropical crops. Among the known works, there is not a single development that could be directly used to calculate the thermal characteristics of trench type solar greenhouses. Physical characteristics are considered, a mathematical model of heat engineering characteristics in a classical form for creating a microclimate in a solar greenhouse is compiled.

The calculation of the heat balance of a trench-type solar greenhouse is presented as a system of heat balance equations for a solar airspace structure, for a time interval dτ, taking into account additional heating in kWh, which can be written as:

$$dQob + dQ\,p + dQw + dQt + dQst + dQp + dQa + dQp = 0 \quad (1)$$

where dQob is the heat dissipation of the heating system; dQ p is the heat flux of solar radiation entering the solar structure; dQw.t - the amount of heat given to the environment as a result of air exchange and heat transfer through the fences; dQst = dQ * st + dQost - heat flow into the wall; dQp = dQp * + dQpo - heat flow into the soil, dQ * p (st), dQp (st) o - heat flux to the illuminated and unlit parts of the wall and soil; dQ is the heat flux accumulated in the air; dQp - heat flux on the vegetation cover (provided that the greenhouse is full of plants). Unit of measurement kWh per area. The heat balance equation for the soil surface and the wall is written in a similar way, as the heat balance equation for the soil, the wall of its illuminated and unlit parts.

As a result of mathematical transformations of Equation (1), the temperature regime of the solar greenhouse in the temporary total heat flow has the form [6]:

$$\theta_{\scriptscriptstyle B} = \int_o^{\tau} I\,(\delta)\exp[-h(\tau-\delta)\,]d\delta - \sum_{i=1}^{4}\frac{Bi\,(\tau)}{R_i}, \quad (2)$$

Studies of a complex and simplified mathematical model of the thermal engineering parameters of a trench solar greenhouse have been carried out. The obtained calculation results showed that a complex and simplified mathematical model adequately reproduces the results of the experiment, with an accuracy: a complex model - 12.35%; simplified - 23.11%. Similarly, a mathematical model of heat and mass transfer and determination of the temperature of the leaf surface of a plant in a solar greenhouse was compiled and considered. The physical model of thermal engineering processes occurring in a trench type solar greenhouse, taken in the calculations, is shown in detail in the monograph.

On the basis of scientifically substantiated results and mathematical modeling of thermal engineering processes, nomograms were created, see Figure 3, empirical expressions 3-8 and geographic information technological maps of the optimal zoning of solar greenhouses in the country, see Figures 4 and 5.

The nomogram for determining the air temperatures in the greenhouse depending on the amount of incoming solar radiation in the Ahal regions of Turkmenistan are shown in Figure 3, similar nomograms are compiled for the Dashoguz, Lebap and Balkan regions and are given in monographs [6].

Taking into account the heat engineering parameters, empirical formulas were obtained, expanded in Fourier series for the outside air temperature Tn, direct solar radiation I, soil and trench walls, have the form:

$$T_{\scriptscriptstyle H} = 12{,}6 + 10\cos(0{,}26t + 0{,}18) + 3{,}27\cos(0{,}52t - 0{,}44) + 1{,}39\cos(0{,}78t + 0{,}23)\,, \quad (3)$$

$$I = 129{,}9 + 217{,}9\cos(0{,}26t + 0{,}13) + 120{,}4\cos(0{,}52t - 0{,}26) + 26{,}9\cos(0{,}78t - 0{,}3). \quad (4)$$

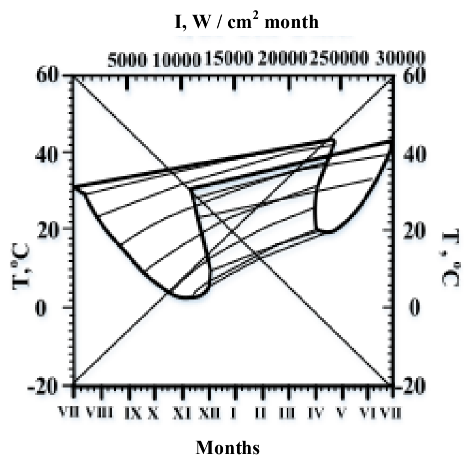

Figure 3. Nomogram for determining the air temperature depending on the incident solar radiation for the Akhal velayat (region)

Substituting Tn and I into expressions (3-4), we obtain dependencies describing the temperature regime of air and soil:

$$T_B = 16{,}2 + 8{,}3\cos(0{,}26t + 0{,}28) + 2{,}8\cos(0{,}52t - 0{,}08) + 0{,}97\cos(0{,}78t - 1{,}42); \quad (5)$$

$$T_{п}|_{x=0} = 21{,}1 + 8{,}59\cos 0{,}26t + 3{,}19\cos 0{,}52t + 0{,}72\cos 0{,}78t; \quad (6)$$

$$T_{п}|_{x=0,1} = 19{,}58 + 3{,}78\cos 0{,}26t + 1{,}01\cos 0{,}52t + 0{,}17\cos 0{,}78t. \quad (7)$$

Equations for the walls of the solar greenhouse trench are described similarly.

The compiled geoinformation map of the average isotherm of the outside air and the trench type solar greenhouse in the month of January (marked in red), similarly the map for the month of July is shown in Figure 4 a, b. The results of implementation and commissioning are confirmed by acts, research protocols, certificates. Study of the energy parameters of the solar module. To create a solar photovoltaic station, experimental studies of the volt-watt (VVC) and volt-ampere characteristics (VAC) of modules of various foreign companies (Japan, Russia, Iran) have been carried out.

Research of photomodules was carried out in different climatic conditions and seasons during the day, with a change in the angle of inclination, orientation with tracking and without tracking, while studying the energy characteristics of: solar radiation; optimal current, short-circuit current; optimal voltage and open circuit voltage; optimal power and efficiency.

Development of a geographic information map for the placement of solar photovoltaic water-lifting units (SHEP) in the Karakum desert. All livestock settlements in the Karakum Desert have wells far from power lines, their water reserves are estimated at 80 km^3, the cost of 1 km of power lines is 18 - 25 thousand US dollars, the construction of power lines is not economically profitable. On the territory of Turkmenistan there are more than 5,000 wells with a depth of 5 - 250 m. The load capacity of the pump has been determined depending on the pressure at various capacities. On the basis of the terrain, depth, flow rate of wells, a geoinformation technological cartogram of the location of the NEFU according to the power of the generated energy was compiled and introduced, depending on the depth of the wells of the desert pasture territories of the Karakum. On the basis of the above scientific research, the SFED was developed, created and put into operation in the Garygul settlement in the Central Karakum at the research base of the National Institute of Deserts, Flora and Fauna (NIPRiZhM) 100 km from Ashgabat.

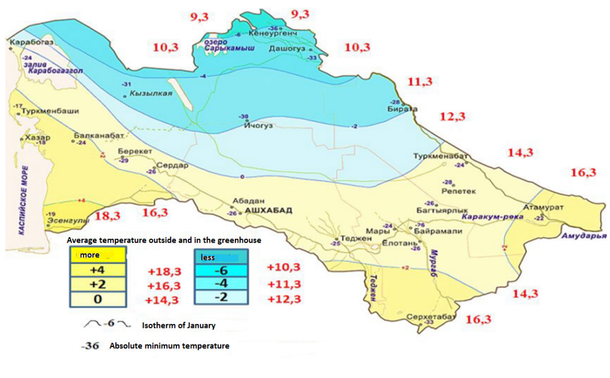

a)

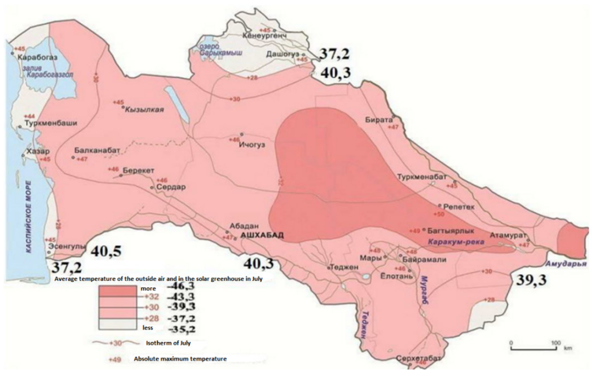

b)

Figure 4. Map of the average isotherm of the outside air and trench type solar greenhouse in January (a) and July (b) by regions of Turkmenistan

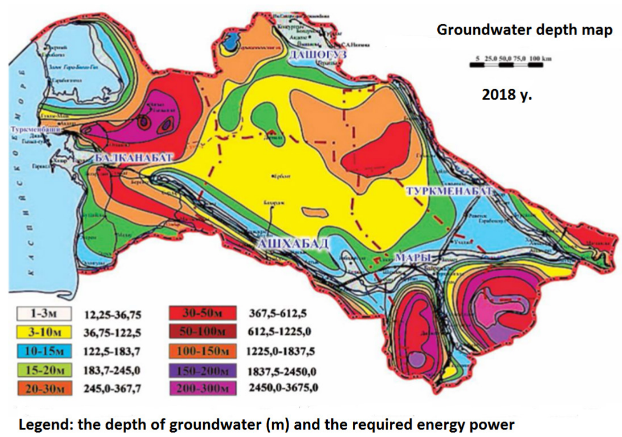

Figure 5. Geo-information technological map, placement of SFEU according to the power of generated energy, depending on the depth of wells in the pasture areas of Turkmenistan

The total power of the installation is: 450 W, with a pressure of 30 m. The developed scheme of the SFVU and the automated control system are given in my scientific articles and monographs.

Implementation act, certificate of scientific and technical use of the results of work, test report, photographs in the thesis attachment.

The developed installation can be used for water supply and other facilities [3-8].

4. The Results of Scientific Research

On the basis of scientifically substantiated systematized energy resources, potentials and implemented energy technologies based on RES for Turkmenistan, the following results were obtained:

Solar energy

Gross resources in kWh /(m^2 year) in the regions are equal: North - 1757.4; South-east - 1895.9; Central Karakum - 1844.6; South -1725.0; West -1685.4.

Technical potentials of conversion into heat energy and electrical energy in kWh/(m^2 year) in the regions, respectively: North - 1227.587 and 244.84; South-east - 1296.78 and 248.55; Central Karakum - 1256.44 and 242.44; Southern - 1234.46 and 225.29; West -1177.12 and 222.6.

Economic potentials from conversion to thermal and electrical energy are in kg of fuel equivalent per year: North - 490.9 and 97.9; Southeast - 518.7 and 99.44; Central Karakum - 502.6 and 96.98; South - 493.8 and 90.14; Western - 470.9 and 89.1.

Environmental indicators: the reduction of emissions of various harmful substances into the environment when using a solar photovoltaic station will be in the Central Karakum with an annual electricity generation from 1 m^2 - 242.44 kWh /year, fuel economy - 96.98 kg of fuel equivalent / year, emission reduction will be, kg / year: sulfur dioxide SO_2 - 2.01; nitrogen oxide NOx - 1.08; carbon monoxide CO- 0.1401; methane CH_4 0.296; carbon dioxide CO_2 - 155.08; solids - 0.211175; when converting to thermal energy from 1 m^2 - annual production is 1256.44 kWh /year, fuel consumption saving - 502.60 kg of fuel equivalent / year, emission reduction will be, kg / year: SO_2 - 10.44; NOx 5.624; CO 0.726; CH_4 1.53; CO_2 - 803.68; solids - 1.094.

5. Conclusions

Based on the analysis of the climatic characteristics of Turkmenistan, water resources, groundwater and the flow rate of the wells of the desert, a geoinformation technological map of the location of a solar photovoltaic water-lifting unit according to the power of the generated energy, depending on the depth of the wells in the pasture territories of Turkmenistan, was compiled. The use of cartographic material made it possible to calculate energy resources, reduce greenhouse gas emissions and reduce the consumption of fossil fuels for the development of 40 million hectares of pasture areas of the country.

The created and put into operation a solar photovoltaic water-lifting unit (SHPH) in the Central Karakum Desert on the experimental base of the National Institute of Deserts, Flora and Wildlife saves 12.0 tons of fossil fuel per year, makes a profit of 3830 US dollars while reducing CO_2 emissions by 38, 4 tons. Taking into account the priorities and prospects for the use of energy technologies based on RES in Turkmenistan under the Clean Development Mechanism (CDM) and the possibility of reducing greenhouse gas emissions in the fuel and energy complex, the areas for the development of solar energy and indicators of its energy efficiency have been identified. With the creation of a plant in Turkmenistan for the production of SFEU with an annual capacity of 20 MW and an annual output of USD 14 million, the expected economic effect from the introduction of the plant's products will amount to USD 12 million per year, fossil fuel savings - 3554.4 t u.t. in year. With an annual intake of solar radiation of at least 1200 kWh / m^2 and the efficient use of this energy, it will be possible to provide up to 25% of heat consumption in heating systems, up to 50% in hot water supply systems and up to 75% in air conditioning systems, reduce the consumption of fossil fuel and to ensure the saving of fuel and energy resources of 2364 thousand tons of fuel equivalent. or 52.6%, including in rural areas 1110.6 thousand tce. tons or 61.5%.

References

[1] Berdymukhamedov, G.M., 2010. State Regulation of Socio-Economic Development of Turkmenistan vol. I / G.M. Berdimuhamedov –- Ashgabat: Turkmen State Publishing Service. pp. 498.

[2] Berdymukhamedov, G.M., 2018. Turkmenistan on the way to achieving the Sustainable Development Goals / G.M. Berdimuhamedov - Ashgabat: Turkmen State Publishing Service. pp. 468.

[3] Strebkov, D.S., Pendzhiev, A.M., Mamedsakhatov, B.D., 2012. Development of solar energy in Turkmenistan. - Moscow: GNU VIESH. pp. 498.

[4] Pendzhiev, A.M., 2012. Climate change and the possibility of reducing anthropogenic pressures. - Germany: LAP LAMBERT Academic Publishing. pp. 164.

[5] Pendzhiev, A.M., 2014. Ecological problems of the development of deserts. - Germany: LAP LAMBERT Academic Publishing. pp. 226.

[6] Pendzhiev, A.M., 2018. Agrotechnics of growing a

melon tree in protected ground conditions: monograph / A.M. Pendzhiev. -Moscow: Rusays. pp. 222.
[7] Pendzhiev, A.M., Penzhieva, D.A., 2015. Resources and efficiency of geothermal water use ": monograph / - Germany: LAP LAMBERT Academic Publishing. pp. 224.
[8] Pendzhiev, A.M., 2017. Basics of GIS in the development of renewable energy: monograph / A.M. Pendzhiev - Germany: LAP LAMBERT Academic Publishing. pp. 308.

CIENTIFIC Publishing Limited

New Energy Exploitation and Application

http://ojs.ukscip.com/index.php/NEEA/issue/view/2

CASE

The Performance Evaluation of Ventilated Windows in the Simultaneous Improvement of Energy Efficiency and Indoor Air Quality in Office Buildings: A Case Study

Farid Khalvati   Amir Omidvar*

Department of Mechanical Engineering, Shiraz University of Technology, Shiraz, Iran

Received: 19 December 2021; **Accepted:** 22 January 2022; **Published Online:** 24 January 2022

Abstract: Energy efficiency and indoor air quality (IAQ) are two crucial required features in a building. Simultaneous improvement of energy efficiency and IAQ in a building can pave the way for obtaining a green building certification. This paper examined the performance of the airflow windows' supply and exhaust operating modes in energy-saving and providing IAQ criteria. The analytical zonal model coupled with the airflow network model was used to evaluate the system's thermal performance and the induced airflow. The simulation was done for an office building located in Shiraz, Iran. The results showed that the energy performance of ventilated windows is positive in nine months of the year. Compared to a conventional double-glazed window, the maximum energy savings is about 10%, which occurs in August. It is predicted that using ventilated windows in office buildings in Shiraz can improve the window's thermal performance by an average of about 5%. The results also showed that ventilated windows could provide the fresh air needed for the building in 250 days of the year to achieve the desired IAQ index (based on ASHRAE 62.1 standard). Furthermore, the effects of glass aspect ratio, airflow channel thickness, and the size of inlet/outlet openings on energy efficiency and IAQ of the suggested window were studied. Results indicated that in the climatic conditions of Shiraz, the exhaust operating mode is much more efficient than the supply mode.

Keywords: Ventilated window, Airflow window, Energy efficiency, Indoor air quality

1. Introduction

Indoor Air Quality (IAQ), as an essential part of Indoor Environmental Quality (IEQ), has a significant effect on the health and productivity of the building occupants. Poor indoor air quality has been connected to Sick Building Syndrome (SBS), lower productivity, which can be harmful to vulnerable groups such as children, young adults, the elderly, or those suffering chronic respiratory and cardiovascular diseases [1].

Keeping the air exchange rate between outdoors and indoors at an acceptable level is an effective solution to improve IAQ. The required exchange rate can be provided by a mechanical ventilation system or natural ventilation through doors, windows, and purpose-designed openings. However, providing the air exchange rate to improve

*Corresponding Author:
Amir Omidvar,
Department of Mechanical Engineering, Shiraz University of Technology, Shiraz, Iran;
Email: omidvar@sutech.ac.ir

DOI: https://doi.org/10.54963/neea.v1i1.12

IAQ through the existing methods often increases energy consumption [2]. According to documents produced by international organizations such as International Energy Agency (IEA) [3], ASHRAE [4], and CEN [5], regulations and advice, and guidelines were provided to target the IAQ/energy efficiency issue. Thus, finding strategies for achieving a satisfactory balance between good indoor air quality and rational energy use is a priority for researchers and designers.

Ventilated window is a novel design to solve this issue. Its structure allows exchanging air between outdoors and indoors while reducing the building cooling and heating loads resulting from the window [6]. This feature also makes the ventilated window an attractive passive system for net-zero energy or green buildings.

While most of the researchers working on the ventilated window focused on evaluating thermal performance and energy efficiency [7-12], The IAQ and energy consumption analysis has been the subject of limited studies. Gosselin and Chen [6] carried out experimentally validated computational fluid dynamics (CFD) simulations on a proposed dual airflow window to optimize the window design. Although they claimed that their proposed ventilated window improves IAQ, no quantitative results in IAQ parameters were reported. Zhang et al. [13] studied the influence of ventilated windows on indoor $PM_{2.5}$ and CO_2 concentration and the overall energy consumption. They reported that the increase of energy consumption due to indoor air quality improvement is inevitable for their specific proposed ventilated window.

Since ventilated window proved itself as an energy-efficient system applied in the building, it is necessary to evaluate its efficiency to provide the required IAQ and recognize the parameters influencing the interaction between IAQ and energy efficiencies. A practical and straightforward approach to assess the IAQ is the determination of the minimum ventilation rate. ASHRAE 62.1 [4] is a well-known reference to follow this approach. The present work aimed at assessing the performance of the naturally ventilated window in energy-saving and provision of IAQ requirement according to ASHRAE 62.1 [4]. First, the annual energy saved by the naturally ventilated window was calculated for a case study.

Furthermore, the adequacy of the induced airflow rate to provide the required fresh air was evaluated according to ASHRAE 62.1 standard [4]. In addition, a parametric study focusing on geometric factors was carried out, and the variation of each two aspects of interest was described. It is hoped that the present results can provide a more detailed picture of the benefit of using the ventilated windows in practice.

2. Description of the Ventilated Window

The subjected naturally ventilated window is composed of two parallel glass panes separated by an air cavity. As shown in Figure 1, air enters the channel through the inlet below and exits through the outlet above. Depending on the inlet and outlet of the airflow duct, four different operating modes can be defined for ventilated windows: supply mode, exhaust mode, indoor air curtain mode, and outdoor curtain mode. In the two modes of "supply" and "exhaust", the indoor and outdoor environments are connected, but these two environments are separate in the other two modes.

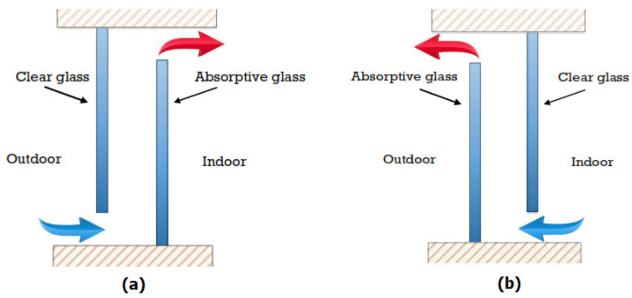

Figure 1. Schematic of the ventilated window: a) supply mode, b) exhaust mode.

For the exhaust mode, which is suitable for summer, the exterior sheet is a single pane of heat-absorbing glass, and the interior one is clear glass. However, for the supply mode used in winter, the sort order of glasses is reversed (see Figure 1). The supply operating mode can preheat the inlet air and compensate for part of the heating load of the indoors. In the naturally ventilated window, wind and buoyancy force due to the temperature difference of glass panes and air are driving forces of flow in the channel. The performance of a naturally ventilated window is the function of outdoor conditions such as velocity and orientation of wind, outdoor temperature, and solar irradiation. Thus, the induced airflow rate changes hourly and is uncontrolled.

3. Mathematical Modelling

3.1 Thermal Modelling

The present work uses the zonal model coupled with the airflow network model to predict the thermal performance of the ventilated window. In the zonal model, the ventilated window is partitioned into "n" equal sections along the channel, called "zone". As shown in Figure 2, three nodes represent the glass panes and the channel airflow temperatures in each zone. The thermal energy balance equation for each node is written to calculate the nodal temperatures. The energy balance equations are formulated under several simplifying assumptions, common in the most relevant studies [9,14].

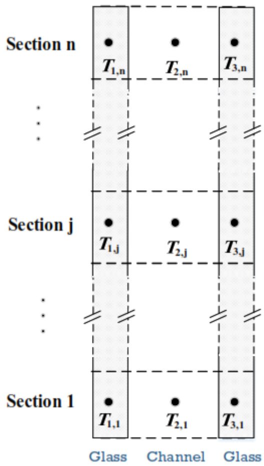

Figure 2. Schematic of the ventilated window discretization [10].

The energy flows of the nodes of section j are shown in Figure 3.

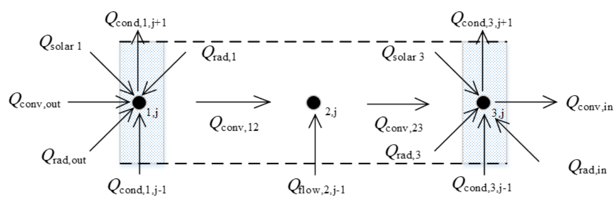

Figure 3. The energy flows of the nodes in each zone [10].

In each zone, writing the energy balance equations for nodes 1, 2, and 3 yields the following equations:

$$\dot{Q}_{\text{conv,out}} - \dot{Q}_{\text{conv 1,2}} + \dot{Q}_{\text{cond 1,j}-1} - \dot{Q}_{\text{cond 1,j+1}} + \dot{Q}_{\text{rad 1}} + \dot{Q}_{\text{rad,out}} + \dot{Q}_{\text{solar 1}} = 0 \quad (1)$$

$$\dot{Q}_{conv\ 1,2} - \dot{Q}_{conv\ 2,3} + \dot{Q}_{flow\ 2,j-1} = 0 \quad (2)$$

$$\dot{Q}_{\text{conv 2,3}} - \dot{Q}_{\text{conv,in}} + \dot{Q}_{\text{cond 3,j}-1} - \dot{Q}_{\text{cond 3,j+1}} + \dot{Q}_{\text{rad 3}} + \dot{Q}_{\text{rad,in}} + \dot{Q}_{\text{solar 3}} = 0 \quad (3)$$

$\dot{Q}_{\text{conv,out}}$, $\dot{Q}_{\text{conv,in}}$, $\dot{Q}_{\text{conv 1,2}}$ and $\dot{Q}_{\text{conv 2,3}}$ are the convective heat transfer that occurred on the window's exterior, interior, and channel surfaces, respectively and are given by Equations (4) and (5) and (6):

$$\dot{Q}_{\text{conv,out}} = h_{\text{conv,out}} A_j\left(T_{1,j} - T_{\text{out}}\right) \quad (4)$$

$$\dot{Q}_{\text{conv,in}} = h_{\text{conv,in}} A_j\left(T_{3,j} - T_{\text{in}}\right) \quad (5)$$

$$\dot{Q}_{\text{conv 1,2}} = \dot{Q}_{\text{conv 2,3}} = h_{\text{conv 1,2}} A_j\left(T_{1,j} - T_{2,j}\right) = h_{\text{conv 2,3}} A_j\left(T_{2,j} - T_{3,j}\right) \quad (6)$$

In these equations, the convective heat transfer coefficients of $h_{\text{conv,out}}$, $h_{\text{conv,in}}$, $h_{\text{conv1,2}}$ and $h_{\text{conv2,3}}$ are calculated according to the conditions of airflow on the window surfaces. Section 3.2 provided more details on their calculations.

$\dot{Q}_{\text{rad,out}}$ and $\dot{Q}_{\text{rad,in}}$ are the radiative heat transferred between the window and surrounding surfaces and are obtained by Equations (7) and (8):

$$\dot{Q}_{\text{rad,out}} = h_{\text{rad,out}} A_j\left(T_{\text{sky}} - T_{1,j}\right) \quad (7)$$

$$\dot{Q}_{\text{rad,in}} = h_{\text{rad,in}} A_j\left(T_{\text{mr}} - T_{3,j}\right) \quad (8)$$

The radiative heat transfer coefficients between surfaces and indoors and outdoors are calculated as follows [9]:

$$h_{\text{rad,in}} = \sigma\varepsilon_4\left(T_{\text{mr}}^2 + T_{3,j}^2\right)\left(T_{\text{mr}} + T_{3,j}\right) \quad (9)$$

$$h_{\text{rad,out}} = 0.5\sigma\varepsilon_1\left(T_{\text{sky}}^2 + T_{1,j}^2\right)\left(T_{\text{sky}} + T_{1,j}\right)\left(T_{\text{sky}} - T_{1,j}\right)/\left(T_{1,j} + T_{out}\right) \quad (10)$$

In Equation (7), T_{sky} is the sky temperature given by [9]:

$$T_{\text{sky}} = 0.0552 T_{\text{out}}^{1.5} \quad (11)$$

Also, T_{mr} in Equation (8) is the mean radiant temperature of surfaces surrounding the interior glass surface, which is assumed to be equal to indoor air temperature [15].

$\dot{Q}_{\text{rad1}}$ and $\dot{Q}_{\text{rad3}}$ are the total of the long-wave radiative heat exchanges between channel-side surfaces of the interested glass pane and the channel-side surfaces of the other zones. Their mathematical formulation are as follows:

$$\dot{Q}_{\text{rad, 1}} = \sum_{i=1}^{n} \frac{\sigma A_{1,j}\left(T_i^4 - T_{1,j}^4\right)}{\frac{1}{F_{1i}} + \frac{1-\varepsilon_i}{\varepsilon_i} + \frac{1-\varepsilon_1}{\varepsilon_1}} \quad (12)$$

$$\dot{Q}_{\text{rad, 3}} = \sum_{i=1}^{n} \frac{\sigma A_{3,j}\left(T_i^4 - T_{3,j}^4\right)}{\frac{1}{F_{3i}} + \frac{1-\varepsilon_i}{\varepsilon_i} + \frac{1-\varepsilon_3}{\varepsilon_3}} \quad (13)$$

where ε is the emissivity of the glass surface. F_{1i} and F_{3i} are the view factors of surfaces exposed to each other.

In Equations (1) and (3), $\dot{Q}_{\text{solar 1}}$ and $\dot{Q}_{\text{solar 3}}$ are the solar radiation absorbed by the outer and inner glass panes, respectively. These terms include two components of direct and diffuse absorption (Equations (14) and (15)).

$$\dot{Q}_{\text{solar 1}} = I_{\text{dir}}\alpha_{\text{dir 1}} + I_{\text{diff}}\alpha_{\text{diff 1}} \quad (14)$$

$$\dot{Q}_{\text{solar 3}} = I_{\text{dir}}\tau_{\text{dir 1}}\alpha_{\text{dir 3}} + I_{\text{diff}}\tau_{\text{diff 1}}\alpha_{\text{diff 3}} \quad (15)$$

I_{dir} and I_{diff} are the direct and diffuse solar irradiations obtained from the climate data of the studied location. a_{dir} and a_{diff} are the direct and diffuse absorption coefficients of the glass panes and $\tau_{\text{dir 1}}$ and $\tau_{\text{diff 1}}$ are the direct and diffuse transmission coefficients of the outer glass pane.

$\dot{Q}_{\text{cond}}$ is the conductive heat transfer between two adjacent zones of glass pane which is obtained readily from Fourier law in a general form of Equation (16).

$$\dot{Q}_{\text{cond i,j}} = \frac{kA_i(T_i - T_j)}{|y_i - y_j|} \tag{16}$$

$y_i - y_j$ is the distance between two adjacent nodes of the glass pane.

Finally, $\dot{Q}_{\text{flow 2,j}-1}$ is the flow energy change through the zone "j" and is given as follows:

$$\dot{Q}_{\text{flow 2,j}-1} = \dot{m}C_p\left(T_{2,j} - T_{2,j-1}\right) \tag{17}$$

C_p is the specific heat capacity of the airflow and $\dot{m}$ is the mass flow rate of channel air. In the forced flow, $\dot{m}$ is determinant, while in natural convection, its magnitude is the function of various parameters such as the temperature of the glass pane and flow and geometric channel dimensions. The present work calculates the mass airflow rate by the airflow network model [16]. This procedure determines the mass flow rate based on pressure distribution along the channel. The details of the airflow network model can be followed in reference [17]. In this situation, the mass and energy balance equations are coupled. First, the mass balance equations are solved using known boundary conditions, and the calculated airflow rates were then inserted into Equations (1) and (3) to calculate the temperatures.

3.2 Convective Heat Transfer Coefficients

The accuracy of zonal model output strongly depends on heat transfer coefficients used in the energy balance equations. Therefore, it is essential to apply proper and validated equations estimating actual thermal and hydrodynamic conditions. As climate conditions such as temperature, velocity, and orientation of wind, and solar radiation are not controllable and change hourly, airflow condition on surfaces of the window is varied and different types of flow (laminar, turbulent, and natural, forced) can occur. Thus, in this work, Nusselt correlations for the possible type of flows were calculated as follows.

Nusselt correlation for the exterior surface of the window, which is valid for both laminar and turbulent regimes, are given as [18].

$$\overline{\text{Nu}}_{mix} = \sqrt[3]{\overline{\text{Nu}}_n^3 + \overline{\text{Nu}}_f^3} \tag{18}$$

In this equation, $\overline{Nu}_n$ is the average Nusselt number of the natural convection and is calculated from the correlation presented by Churchill and Chu [18].

$$\overline{\text{Nu}}_n = \left(0.825 + 0.325\text{Ra}_H{}^{\frac{1}{6}}\right)^2 \tag{19}$$

$\overline{\text{Nu}}_f$ is the averaged Nusselt number of forced convection [19]:

$$\overline{\text{Nu}}_f = \frac{H}{k}(4.7 + 7.6v_s) \tag{20}$$

where v_s is the characteristic velocity of air flowing on the glass surface and is the function of the local wind velocity.

When the surface is windward, v_s can be obtained as [19]:

$$v_s = \begin{cases} 0.5 & ; \quad v \le 2\ \text{m/s} \\ 0.25v & ; \quad v > 2\ \text{m/s} \end{cases} \tag{21}$$

and, for a leeward surface:

$$v_s = 0.3 + 0.05v \tag{22}$$

where v is the local wind velocity obtained by meteorological measurements.

The convective heat transfer on the internal side primarily occurs by natural convection, and rarely by mixed and forced convection. Thus, Nusselt correlation of natural convection for the interior surface can be calculated from Equation (19).

Nusselt correlations used for laminar and turbulent regimes are separated for the channel side of the ventilated window. For laminar flow, the correlation presented by Bar-Cohen [20] was applied (Equation (23)) and for turbulent flow, the correlation suggested by Badr et al. [21] was used (Equation (24)).

$$\overline{Nu}_n = \left(\frac{576}{\text{Ra}_b} + \frac{2.873}{\sqrt{\text{Ra}_b}}\right)^{-0.5} \tag{23}$$

$$\overline{Nu}_n = 0.64\ (\text{Ra}_b)^{0.27} \tag{24}$$

3.3 Calculation of Total Heat Gain

To determine the thermal performance of windows, the total heat gain is an illustrative parameter. The total heat gain for the ventilated window includes three parts (Equation (25)); one part is the heat transfer due to the temperature difference between the interior glass surface and indoors, and one part is the heat transfer due to solar irradiation directly transmitted to the indoor space. The third part appears for the supply mode of the ventilated window in which the outdoor air is preheated while passing through the window channel before entering the room. Equations (26) to (28) define these three parts of the total heat gain. T_{outlet} in Equation (28) is the air temperature exit the channel entering the room.

$$Q_{\text{gain}} = Q_{\text{solar}} + Q_{\Delta\text{T}} + Q_{\text{preheat}} \tag{25}$$

where

$$Q_{\text{solar}} = \int_{t_1}^{t_2} \sum_{j=1}^{n} A_j\left(I_{\text{dir}}\tau_{\text{dir}} + I_{\text{diff}}\tau_{\text{diff}}\right)_j dt \tag{26}$$

$$Q_{\Delta T} = \int_{t_1}^{t_2} \sum_{j=1}^{n} A_j \left(h_{\mathrm{rad,in}} + h_{\mathrm{conv,in}}\right)_j \left(T_{3,\mathrm{j}} - T_{\mathrm{in}}\right) dt \tag{27}$$

$$Q_{\mathrm{preheat}} = \int_{t_1}^{t_2} \dot{m} C_p \left(T_{\mathrm{outlet}} - T_{\mathrm{in}}\right) dt \tag{28}$$

In the present work, energy saving is the result of the difference between the total heat gain of the equivalent double-glazed window and the ventilated window.

3.4 Requirements for Indoor Air Quality

According to standard ASHRAE 62.1 [4], the design zone outdoor airflow, i.e., the outdoor airflow provided to the zone by the supply air distribution system, shall be determined according to Equation (29).

$$\dot{V}_{oz} = \frac{\dot{V}_{bz}}{E_z} \tag{29}$$

$\dot{V}_{bz}$ is the breathing zone outdoor airflow, which is the design outdoor airflow required in the breathing zone of the occupiable space or spaces in a zone. This parameter is determined as:

$$\dot{V}_{bz} = R_p P_z + R_a A_z \tag{30}$$

where P_z and A_z are zone population and zone floor area. R_P and R_a are outdoor airflow rates required per person and per unit area respectively and determined from tables given in standard ASHRAE 62.1 [4].

E_z is Zone Air Distribution Effectiveness and defined as a measure of how effectively the zone air distribution uses its supply air to maintain the acceptable air quality in the breathing zone. The value of E_z is listed in table 6-2 of standard ASHRAE 62.1 [4].

4. Validation of the Zonal Model

In order to verify the zonal model coupled with airflow network model, the experimental data reported by Chow et al. [14] are used. Chow et al. carried out an experiment of a ventilated window in Hong Kong for three consecutive summer days. The studied window is 1.95 m in height and 0.88 m in width composed of an outer absorptive glass pane and an inner clear glass pane. The cavity thickness is 0.035 m.

Figure 4 compares the calculated and the measured temperatures of the absorptive and clear glass panes. The graphical plots indicate that the zonal model can soundly predict changes in glass temperature. However, it is found under-estimation in all hours of simulation. It is probably due to unpredictable weather conditions and the effect of the window configuration, such as louvers installed for intake and exhaust and the frame. The mean and maximum deviations of the temperatures of absorptive and clear glasses are (0.42 and 2.3) ℃ and (0.23 and 1.2) ℃ , respectively.

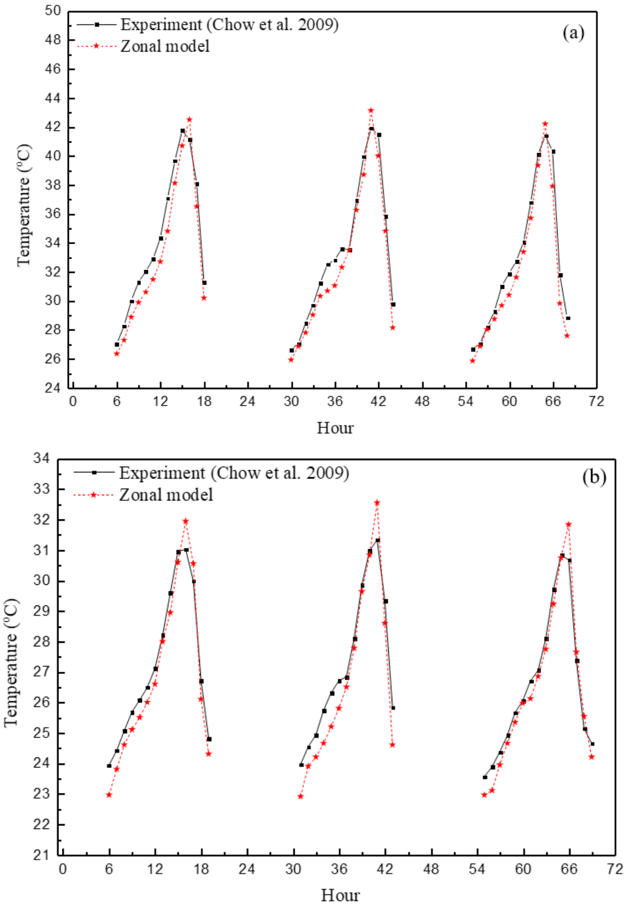

Figure 4. Comparison of glazing surface temperature of the present zonal model with the results reported by Chow et al. [14]: a) absorptive glass pane, b) clear glass pane.

5. Results and Discussion

Consider a 6 m × 5 m ×3 m office room. This room carries a 3 m^2 window at the center of the external wall. According to Iranian national building regulation, this considered area of the window-to-floor ratio of 0.1. This regulation states that rooms should be provided with natural lighting through windows as much as possible. Therefore, the total window area should be less than 10% of the floor area in each space. The window in the current study was taken as facing south to have a maximum solar thermal load. The indoor temperature setpoints are 20 °C in winter (from November to April next year) and 24 °C in summer (from April to October). According to standard ASHRAE 62.1 [4], Rp is 2.5 L/s for each person, and Ra is 0.3 L/sm^2. Considering the occupant density of 5 persons per 100 m^2, the breathing zone outdoor airflow is calculated at 12.75 L/s.

Assuming supply is drawn in on the opposite side of the room from the exhaust, the zone air distribution effectiveness, Ez, is equal to 0.8 for both winter and summer operations. Therefore, in the current study, the overall airflow rate required to meet IAQ is 15.9 L/s. In this work, the WINDOW software (Version 7.2) was used to acquire the glass radiative properties required for the zonal model. Table 1 shows the normal-incident optical characteristics of the window glasses.

Table 1. The normal-incident optical characteristics of the window glasses.

	a	ρ	τ	ε
absorptive glass	0.508	0.054	0.438	0.84
clear glass	0.091	0.075	0.834	0.84

The selected city for simulation was Shiraz, located in the south of Iran. The data library reported by Iran Meteorological Organization was the source of the required weather data, including direct and diffuse solar radiation, dry bulb temperature, and velocity and direction of the wind. Also, calculations were done hourly and under quasi-steady conditions.

5.1 The Thermal Performance of Natural Ventilation via Ventilated Window

As stated in section 2, natural ventilation via the ventilated window is possible for both modes of supply and exhaust. The chosen city to study was Shiraz, the city of Iran with a hot semi-arid climate. As ventilated windows are more efficient in the day than night due to solar radiation and the working time of offices is usually from morning to afternoon, the time interval of the study is limited to 6:00-18:00. The window's aspect ratio is 1.5, and the channel thickness is 10 cm. The simulation was conducted for all hours of the year. The simulation results of monthly energy saved are shown in Figure 5. Blue and red columns, respectively, indicate the results of supply and exhaust modes.

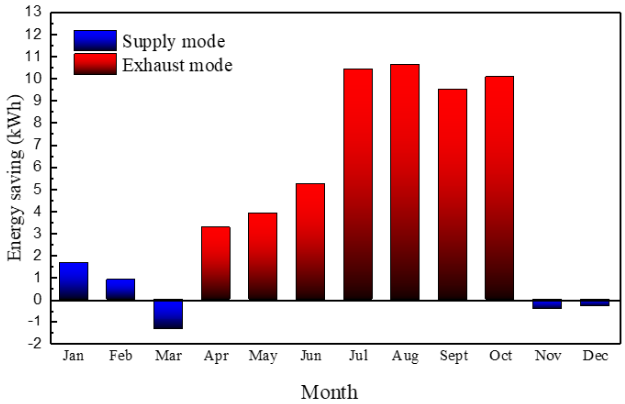

Figure 5. The monthly energy saved for the naturally ventilated window.

As shown in Figure 5, the exhaust mode is considerably more energy-efficient than the supply mode for Shiraz. The energy-saving in the three months of March, November, and December is negative, which is meant that the energy consumption increases in these months. However, this increase in energy consumption is negligible, so that the percentage of increase is less than 2% (see Table 2). In addition, exhaust mode has better performance in three months of summer than in spring. It is due to the higher temperature and solar irradiance in the summer months rather than the spring months. The annual energy saving obtained using the naturally ventilated window is 53.3 kWh.

In addition to energy-saving efficiency, the ventilated window has proved itself a helpful system in providing airflow required for IAQ. Figure 6 shows the airflow rate passed through the ventilated window in the first five days of July. After sunrise, the air starts to flow in the channel, as can be seen. As the hour reaches noon, the flow rate increases and then falls to zero near sunset. Considering

Table 2. The percentage of the monthly energy saving compared to the double-glazing window.

Month	Jan	Feb	Mar	Apr	May	Jun	Jul	Aug	Sep	Oct	Nov	Dec	Total
Energy saving (%)	5.4	1.8	-1.9	4.3	5.6	6.3	9.6	9.7	7.8	7.3	-0.53	-0.63	5.3

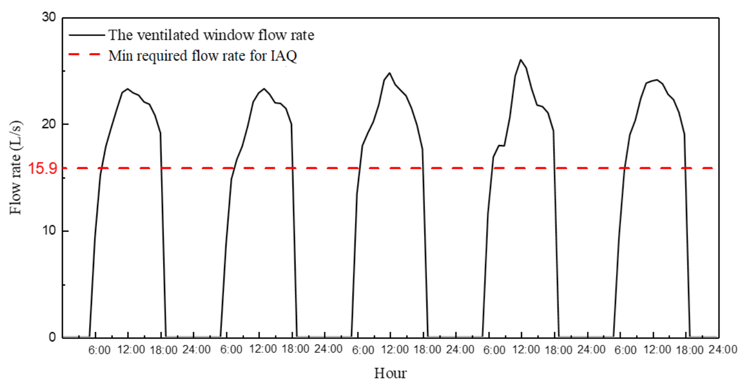

Figure 6. The airflow rate passed through the ventilated window in the first five days of July.

the 15.9 L/s as the minimum airflow rate required to provide fresh air of the office space, the ventilated window can induce the required airflow from morning to afternoon, covering offices' working hours. It should be mentioned that the inlet and outlet of the channel are considered closed during the night, and the window acts as a double-glazed window.

In order to have a better view into the system efficiency in IAQ subject, the histogram of the hours in which the airflow rate is higher than that required during a year is plotted as Figure 7.

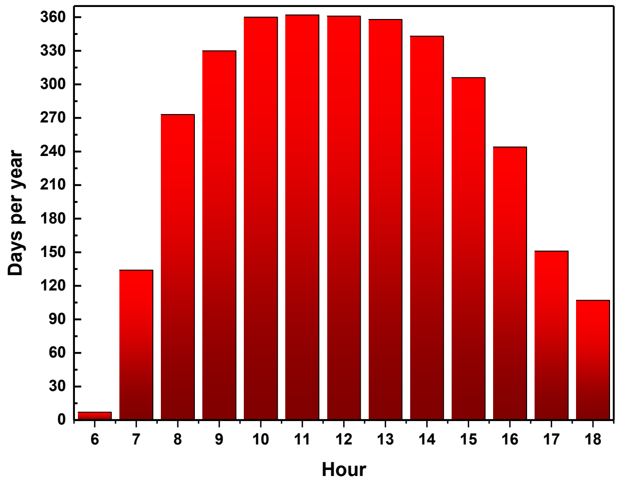

Figure 7. The histogram of the hours when IAQ requirement met during a year.

Midday hour, 12:00, experiences the most days of the year for providing minimum fresh air. It is evident that the solar radiation exposure to the southern window is the maximum around noon and the natural ventilated window has the maximum efficiency in generating the airflow. In addition, there are over 240 days between 8:00 and 16:00 when the generated airflow is higher than that required for IAQ.

5.2 Parametric Study of the Ventilated Window

Geometry has a primary role in the thermal performance of the ventilated window. The proper geometrical design of the ventilated window can efficiently improve its functionality. In the present study, the effect of the geometry characteristics (including the channel thickness, the thickness and aspect ratio of the glass, and the inlet and outlet size) on the thermal performance and IAQ was investigated. The outputs considered for evaluation are:

1) The annual thermal energy saved by the ventilated window is representative of thermal performance.

2) The number of days during the year in which the ventilated window provides the minimum airflow rate during the working time of the office (8:00 -16:00) as representative of IAQ.

Figure 8 shows the effect of the glass aspect ratio on the two above outputs. As can be seen, the thermal energy saved decreases as the aspect ratio increases. Considering the glass area constant, increasing aspect ratio increases the glass height and decreases its width, consequently decreasing the channel Rayleigh number. When the channel Rayleigh number reduces, the channel airflow carries less thermal energy. Thus, the more solar energy absorbed by the inner glass is transferred indoors. Changing the aspect ratio from 0.5 to 2 lessens the energy saving by 13%. A similar trend can be seen for the IAQ index. A higher aspect ratio weakens the buoyancy force to induce airflow to the channel.

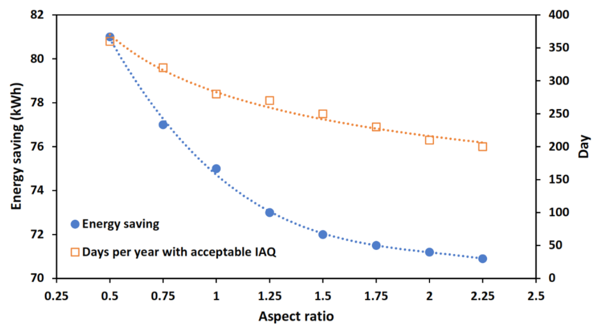

Figure 8. The effect of glass aspect ratio on energy saving and IAQ.

The effect of the channel thickness is described in Figure 9. As shown, increasing the channel thickness results in the increase of all outputs. From the energy and airflow points of view, the channel thickness has the determining effect on generating buoyancy force. It is explainable mathematically in channel Rayleigh number definition where channel thickness appears with fourth power ($Ra_b = \frac{g\beta\Delta T}{\vartheta\alpha}\frac{b^4}{H}$). Since natural convection relies directly on the Rayleigh number, the increase of channel thickness leads to increasing the energy-saving and airflow rate.

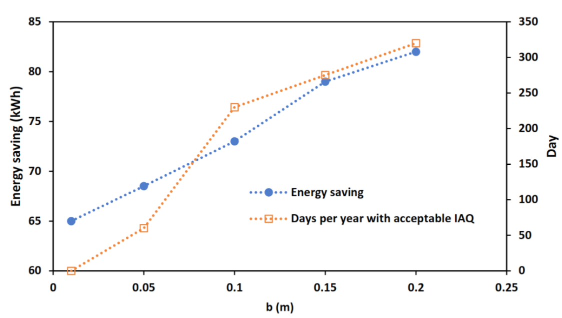

Figure 9. The effect of channel thickness on energy-saving and IAQ.

Inlet and outlet size is another factor influencing the window performance. In the present study, both inlet and outlet sizes are assumed the same. As depicted in Figure 10, energy-saving is augmented as opening height increases. It is expected that the airflow passes more easily through the channel when the local flow resistance of the outlet and inlet is reduced by increasing the inlet and outlet height. Openings act as valves and control the airflow rates. To provide airflow rate required for IAQ, it is necessary to determine a minimum size for openings. As can be seen in Figure 10, the opening size below 5 cm does not meet the minimum airflow rate of 15.9 L/s.

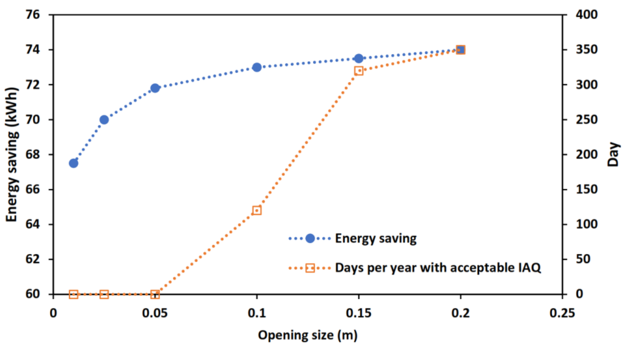

Figure 10. The effect of opening size on energy saving and IAQ.

6. Conclusions

The present work examined the thermal performance of the naturally ventilated window and its capability to provide adequate fresh air flow rate according to indoor air quality standards. Zonal model coupled with airflow network model was used to simulate the ventilated window's thermal performance and airflow rate. The simulation was done for Shiraz, and the monthly energy-saving and the hourly airflow rate induced by the ventilated window were evaluated. It was found that the summer performance of the ventilated window is more efficient than the winter performance. Compared to the double-glazed window, the maximum percentage of energy-saving is obtained in August with 9.7%, while the ventilated window deteriorated in March with 1.9% more heat gain. An annual energy saving of 5.3% is achieved.

The airflow rate induced naturally by the ventilated window changes hourly so that the flow starts with sunrise and increases to its maximum value around noon and then falls as reaching sunset. Considering 15.9 L/s as the minimum airflow rate to meet the IAQ standard of ASHRAE 62.1 and the working time of the office between 8:00 and 16:00, the ventilated window can supply the required fresh air for 259 days of the year.

Furthermore, a parametric study was done to study the effect of the channel thickness, window aspect ratio, and opening size on the thermal performance and index of the number of days with minimum airflow rate covering the office working time. It was found that the increase in the channel thickness and opening ratio leads to the energy-saving and IAQ index whilst the aspect ratio increase causes the energy-saving and IAQ index to reduce.

Declaration of Interests

The authors declare that they have no known competing financial interests or personal relationships that could have appeared to influence the work reported in this paper.

Nomenclature

A	Area (m^2)	Subscripts	
C_p	Specific heat (J/kgK)	conv	Convection
E_z	Zone Air distribution effectiveness	b	Channel thickness
F	View factor	diff	Diffuse
h	Convective heat coefficient (W/m^2K)	dir	Direct
I	Solar radiation (W/m^2)	rad	Radiation
k	Conductivity (W/mK)	cond	Conduction
$\dot{m}$	Mass flow rate (kg/s)	H	Channel height
Nu	Nusselt number	in	Indoor
$\dot{Q}$	Heat flux (W)	out	Outdoor
Ra_b	Channel Rayleigh number $\frac{g\beta\Delta T}{\vartheta\alpha}\frac{b^4}{H}$	D_h	Hydraulic diameter
Ra_H	Rayleigh number $\frac{g\beta\Delta TH^3}{\vartheta\alpha}$	mr	Mean radiant
T	Temperature (℃)	f	Forced convection
$\dot{V}$	Volume flow rate (m^3/s)	n	Natural convection
		mix	Mixed convection
Greek symbols		s	Surface
α	Absorption coefficient	bz	Breathing zone
σ	Stefan-Boltzmann's constant	oz	Outdoor zone
ε	Emissivity		
τ	Transmission coefficient		
ρ	Reflection coefficient		

References

[1] Cincinelli, A., Martellini, T., 2017. Indoor Air Quality and Health. Int. J. Environ. Res. Public Health. 14(11), 1286.
DOI: https://doi.org/10.3390/ijerph14111286.

[2] European Collaborative Action, 1996. Indoor Air Quality and the Use of Energy in Buildings. http://seedengr.com/Indoor%20air%20quality%20and%20it's%20impact%20on%20man.pdf (Accessed 13 May 2021).

[3] Hobday, R., 2005. Technical synthesis report, Annex

31, Energy-related environmental impact of buildings, Faber Maunsell Ltd, UK.

[4] ASHRAE, 2013. Ventilation for Acceptable Indoor Air Quality. ANSI/ASHRAE Standard 62.1

[5] CEN, 2014. Ventilation for buildings (CEN/TC 156).

[6] Gosselin, J.R., Chen, Q., 2008. A dual airflow window for indoor air quality improvement and energy conservation in buildings. HVAC&R Research. 14(3), 359-372.
DOI: https://doi.org/10.1080/10789669.2008.10391014.

[7] Chow, T.T., Lin, Z., He, W., Chan, A.L.S., Fong, K.F., 2006. Use of ventilated solar screen window in warm climate. Appl. Therm. Eng. 26, 1910-1918.
DOI: https://doi.org/10.1016/j.applthermaleng.2006.01.026.

[8] Carlos, J.S., Corvacho, H., 2013. Ventilated double window for the preheating of the ventilation air comparison of its performance in a northern and a southern european climate. J. Renew. Energy. 1-12.
DOI: https://doi.org/10.1155/2013/290865.

[9] Zhang, C., Wang, J., Xu, X., Zou, F., Yu, J., 2016. Modeling and thermal performance evaluation of a switchable triple glazing exhaust air window. Appl. Therm. Eng. 92, 8-17.
DOI: https://doi.org/10.1016/j.applthermaleng.2015.09.080.

[10] Khalvati, F., Omidvar, A., 2019. Summer study on thermal performance of an exhausting airflow window in evaporatively-cooled buildings. Appl. Therm. Eng. 153, 147-158.
DOI: https://doi.org/10.1016/j.applthermaleng.2019.02.135.

[11] Khalvati, F., Omidvar, A., Hadianfard, F., 2021. Study on summer thermal performance of a solar ventilated window integrated with thermoelectric air-cooling system. Int. J. Energy Environ. Eng.
DOI: https://doi.org/10.1007/s40095-020-00376-8.

[12] Ghadimi, M., Ghadamian, H., Hamidi, A.A., Fazelpour, F., Behghadam, M.A., 2012. Analysis of free and forced convection in airflow windows using numerical simulation of heat transfer. Int. J. Energy Environ. Eng. 3, 14.
DOI: https://doi.org/10.1186/2251-6832-3-14.

[13] Zhang, N., Jin, W., He, J., 2016. Experimental study on the influence of ventilated window on indoor air quality and energy consumption. Procedia Eng. 146, 296-302.
DOI: https://doi.org/10.1016/j.proeng.2016.06.394.

[14] Chow, T.T., Lin, Z., Pie, G., Chan, A.L.S., Fong, K.F., 2009. A comparative study of PV glazing performance in warm climate. Indoor Built Environ. 18, 32-40.
DOI: https://doi.org/10.1177/ 1420326X08100323.

[15] Hweij, W.A., Al Touma, A., Ghali, K., Ghaddarn N., 2017. Evaporatively-cooled window driven by solar chimney to improve energy efficiency and thermal comfort in dry desert climate. Energy Build. 139, 755-761.
DOI: https://doi.org/10.1016/j.enbuild.2017.01.071.

[16] Jiru, T.E., Haghighat, F., 2008. Modeling ventilated double skin facade-A zonal approach. Energy Build. 40, 1567-1576.
DOI: https://doi.org/10.1016/j.enbuild.2008.02.017.

[17] Clarke, J.A., Hensen, J.L.M., 1991. An approach to the simulation of coupled heat and mass flow in buildings. In: 11th AIVC Conference of Ventilation System Performance. IEA Air Infiltration and Ventilation Center, Belgirate. pp. 339-354.

[18] Churchill, S.W., Chu, H.H.S., 1875. Correlating equations for laminar and turbulent free convection from a vertical plate. Int. J. Heat Mass Transf. 18, 1323-1329.
DOI: https://doi.org/10.1016/0017-9310(75)90243-4.

[19] Ito, N., Kimura, K., Oka, J., 1972. A field experimental study on the convective heat transfer coefficient on exterior surface of a building. In: ASHRAE Transactions. 78, part 1.

[20] Bar-Cohen, A., Rohsenow, W.M., 1984. Thermally optimum spacing of vertical, natural convection cooled, parallel plates. In: Transactions of the ASME.

[21] Badr, H.M., Habib, M.A., Anwar, S., Ben-Mansour, R., Said, S.A.M., 2006. Turbulent natural convection in vertical parallel-plate channels. Heat and Mass Transfer. 43, 73-84.
DOI: https://doi.org/10.1007/s00231-006-0084-z.

SCIENTIFIC Publishing Limited

New Energy Exploitation and Application

http://ojs.ukscip.com/index.php/NEEA/issue/view/2

RESEARCH ARTICLE

Computational Investigation of Beryllium and Lithium Performance in Future Fusion Tokamaks

M. A. Bourham[1] B. F. Mohamed[2] N. M. Elbasha[3*]

1. North Carolina State University, Department of Nuclear Engineering, Raleigh, NC 27695, USA
2. Plasma Physics Department, Nuclear Research Centre, Atomic Energy Authority, Cairo, Egypt
3. Physics Department, Faculty of Science, Ain Shams University, Cairo, Egypt

Received: 23 December 2021; **Accepted:** 22 January 2022; **Published Online:** 26 January 2022

Abstract: Low-z materials are exemplary candidates in tiling critical plasma-facing components in future fusion reactors due to their low ablation rates under intense high heat fluxes especially during abnormal and hard disruption events. Beryllium and Lithium as low-z materials show good performance as plasma-facing materials in current tokamak. Future tokamaks will exhibit long duration hard disruptions, which in turn requires further investigation of plasma-facing materials, as Li and Be, to judge their performance and evaluate their erosion rates. Electrothermal plasma capillary discharges are used to simulate the high-heat flux deposition on materials to assess their erosion rates. The electrothermal plasma code ETFLOW, which is written for capillary discharges to predict the plasma parameters and erosion rates is used to simulate the high-heat flux conditions similar to expected disruption events for simulated heat fluxes from as low as ~50 to as high as ~290 GW/m^2 with a reconnoitering of generating the Be and Li plasmas up to the third ionization (Br^{+++}, Li^{+++}). Performance of Be and Li under the lowest capillary discharge currents (50 kA and 100 kA) is almost identical, however, Li shows sharper increase in the plasma pressure, heat flux, total ablated mass and the exit velocities than Be for higher discharge currents (150, 200 and 250 kA). This huge difference between the performance of Li and Be under low and high heat fluxes can be an important issue for the future magnetic fusion reactors.

Keywords: Plasma facing materials, Tokamak, Hard disruptions, The next fusion reactors, The low-z materials

1. Introduction

Magnetic fusion Tokamak reactors like ITER will be the first step to test the viability of fusion and to help solving the engineering problems associated with such reactors. One of the challenges in these devices is the plasma-material interactions (PMI) issues because impurities produced as a result of these interactions deteriorate plasma performance. There is also the effect on the lifetime of the plasma-facing materials (PFMs) due to ablation resulting from high heat flux exposure during normal and abnormal operational regimes. These impurities contaminate the core plasma and dilute the hydrogenic fuel, which gives rise to the loss of energy due to increased Bremsstrahlung radiation.

*Corresponding Author:
N. M. Elbasha,
Physics Department, Faculty of Science, Ain Shams University, Cairo, Egypt;
Email: nermeen_elsayed@sci.asu.edu.eg

DOI: https://doi.org/10.54963/neea.v1i1.17

Most desirable properties of plasma-facing material are the low atomic number, low sputtering yield, high heat capacity, predictable and reliable hydrogen recycling characteristics, high melting and vaporization temperatures, and high thermal conductivity. Consequently, low Z materials are preferred for first wall of fusion reactors like Carbon, Beryllium and Lithium (in the reactor blanket for tritium breeding). Beryllium as a PFM has been used since 1990*s* in the high power fusion devices like JET tokamak [1].

Lithium has strong oxygen getter activity and strong hydrogen retention [2]. Beryllium has the advantage of being a low-Z material so low risk of plasma contamination, non-reactive with hydrogenic isotopes and has good thermal conductivity [3,4], however, its dust is toxic when ablating and expanding into the vacuum vessel of the reactor. Echols and Winfrey conducted computational work using the electrothermal plasma code ETFLOW in the ideal plasma regime for capillary discharge to simulate high heat flux deposition on materials and their ablative behavior [5]. They compared performance of beryllium and lithium at heat fluxes between 10 and 125 GW/m^2 with capillary discharge currents between 9.5 to 76 kA. They reported the highest ablation for beryllium as compared to lithium [5]. The present study compares beryllium and lithium in the non-ideal plasma regime for heat fluxes between 57 and 288 GW/m^2 with capillary discharge currents between 50 to 250 kA over a 120 μs pulse length.

The advantages of beryllium are in its low *Z* number, less fuel dilution and lower radiative power loss. Additionally, its high oxygen gettering ability, and the fact that it does not chemically sputter in hydrogen plasma and its low hydrogen inventory [3,4] encourages many researchers to consider beryllium over other PFM [6]. Hassanein and Ehst compared the performance of Beryllium and graphite under hard disruption conditions expected in ITER by using the A*THERMAL computer code [3]; they found that both beryllium and graphite have advantages and disadvantages depending on the design, engineering and operation [3]. The very strong disruption in the next-step fusion reactors may need more loaded material instead of the current plasma facing materials of C, Be, and W.

In 2007 ITER design review confirmed the selection of beryllium for the first-wall components based on its acceptable effect on plasma performance [6], and the knowledge gained from the JET reactor that uses Be tiles.

Lithium as a low atomic number material has a high latent heat of evaporation, low melting temperature and not a serious source of impurities that induces a rise in Z_{eff}, and several applications in lithium technologies such as Li-pellet injection [7], as well as liquid surface and/or capillary-pore limiters [8-10], which are widely used in contemporary magnetic confinement devices. J. A. Snipes injected solid lithium and boron pellets into TFTR plasma to coat the graphite inner wall bumper limiter with a small amount of lower Z pellet material, which improved the plasma performance and the addition of a small amount of Li on a graphite target reduce the C sputtering yield [7].

V. A. Evtikhin et al. have performed experiment with lithium CPS on the hydrogen plasma accelerator MK-200 where they found that in the vicinity of the CPS surface a dense protective layer of lithium plasma is formed, due to which a solid CPS structure will not be damaged under a short-term high thermal load [11]. Solid CPS filled with liquid lithium(CPS) as a plasma facing material has many advantages such as high resistance to radiation damage and thermal stresses, cracking, melting in steady state and during plasma transitions (disruptions and Edge Localized Modes “ELM”), and possess surface self-regeneration through surface tension forces, which are basically different from the solid material divertor concept

J. S. Hua et al. have performed first experiment of liquid lithium limiter on HT-7 tokamak and reported that the core electron temperature slightly increased, the particle confinement time increased by a factor of 2, and a 20% increase in the energy confinement time [12]. After lithium coating, the hydrogen recycling decreased, and core electron temperature increased significantly by a factor of 2. At the same time, after lithium coating, electron density of edge plasmas obviously decreased while electron temperature slightly increased [12].

Improvement in plasma performance is noticed when coating the graphite inner wall bumper limiter with a small amount of Lithium and Boron which reduces the influx of carbon from the walls so a progress in the wall conditioning is achieved [13].

Our purpose in this research is to judge the performance of Li and Be and evaluate their erosion rates. Electrothermal plasma capillary discharges have been used to simulate the high-heat flux deposition on materials to assess their erosion rates. The electrothermal plasma code ETFLOW, which is written for capillary discharges to predict the plasma parameters and erosion rates, simulates the high-heat flux conditions similar to expected disruption events. It has been used in this study for simulated heat fluxes from as low as ~50 to as high as ~290 GW/m^2 with a reconnoitering of generating the beryllium and lithium plasmas up to the third ionization (Be^{+++}, Li^{+++}).

2. Ideal and Non-ideal Plasma Models in the ETFLOW Computer Code

Collisional processes in plasma determine its electrical conductivity from the electro-ion and electron-electron collisions, as well as contribution for electron-neutral atoms collisions. Collisional processes are ideal for low-density plasmas, however, if the density increases the collision between particles also increases and the mean energy of inter-particle interaction increases.

When the strong potential energy of the interacting particles exceeding their kinetic energies the ideal Spitzer model [14] does not describe the plasma well, and hence there is need for the non-ideal model for high-density plasmas.

High density plasma with non ideal effects is recognized in many natural phenomena and devices, and in nature such as super dense plasma of white dwarfs, the sun and the deep layers of giant planets in the solar system; and in energy-related project devices like pulsed fusion, powerful MHD generators and rocket engines.

The parameter $\gamma = e^2 n^{1/3} / 4\pi\varepsilon_0 k T_e$ defines the plasma to differentiate between ideality and non ideality based on the interaction between the charged particles, Where n is the sum of the electron and ion number densities, k is Boltzmann constant, ε_0 is permittivity of free space, and T_e is the plasma electron temperature. This parameter defines plasma as ideal if $\gamma << 1$ and nonideal for $\gamma > 1$.

The Coulomb logarithm is the main feature difference between the ideal and non-ideal plasma models and is given by $\ln(\Lambda) = \ln(1.23\times10^7 T^{3/2} / n^{1/2}\bar{Z}^{-3/2})$ for ideal plasmas, where T is the plasma kinetic temperature, n is the number density and $\bar{Z}$ is the average charge state. An exact analytical model for the Coulomb logarithm for non-ideal plasma has been derived by Zaghloul et al. [15,16], which replaces the standard Coulomb logarithm and covers the range of ideal and nonideal plasmas and is given by $\ln(\Lambda) = \frac{\pi}{2}\sin(3/2\Lambda)[1 - \frac{2}{\pi}(Si(3/2\Lambda) + \frac{Ci(3/2\Lambda)}{Tan(3/2\Lambda)})]$. Both models, ideal and nonideal Coulomb logarithms, are included in a special routine in the ETFLOW code of the capillary discharge, which simulates typical disruption high heat flux deposition, and calculates the plasma conductivity in the Joule heating term in the energy equation.

This model is effective in calculating the joule heating term in the energy equation for electrothermal plasmas, and covers the entire range from weakly to strongly non-ideal [15,16]. The code also includes the Spitzer ideal model for comparison of the results between ideal and non-ideal plasma regimes.

3. Results and Discussion

Figure 1 shows the plasma pressure of beryllium at the capillary exit, indicating a peak pressure of $3.28\text{x}10^8$ N/m^2 (328 MPa) at 50 kA to $1.16\text{x}10^9$ N/m^2 (1158 MPa) at 250 kA. The pressure peaks at about 15 μs after the peak of the discharge current as the discharge current is the source of Joule heating of the capillary arc, which emits radiant heat flux and initiates surface ablation and ejection of the particulates from the liner material, followed by dissociation and ionization, and hence the pressure buildup follows. At about 50 μs the pressure falls down slowly. Same trends are observed for lithium, as shown in Figure 2. A comparison between Be and Li peak pressures is illustrated in Figure 3, in which it is clear that lithium produces higher pressure at the capillary exit.

It is noticed that the increase in pressure is doubled with the increase in the current. For example, the difference between the exit pressure of Li and Be at 100 kA current is 5.000E+08 while the difference between the exit pressure of Li and Be at 150 kA current is 14.00E+08, however the difference between the exit pressure of Li and Be at 200 kA current is 23.000E+08.

Time evolution of the plasma temperature of Li at the capillary exit is illustrated in Figure 4 for the tested range of peak discharge current 50-250 kA. As noticed the temperature increases continually until 10 μs after that it falls down quickly until all temperatures of all currents have the same value (12,000°K) at the end of discharging. The plasma temperature of Be has different behavior, it falls down slowly at the end of the discharge and each current has different temperature, for example at 50 kA the plasma temperature at 120 μs is 12,000°K while at 250 kA the plasma temperature at 120 μs is 22,500°K.

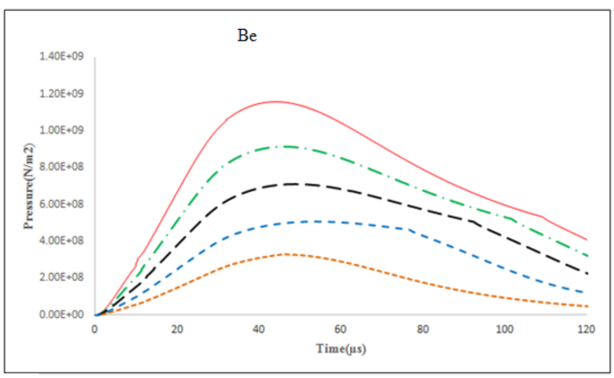

Figure 1. Plasma pressure of beryllium at the capillary exit

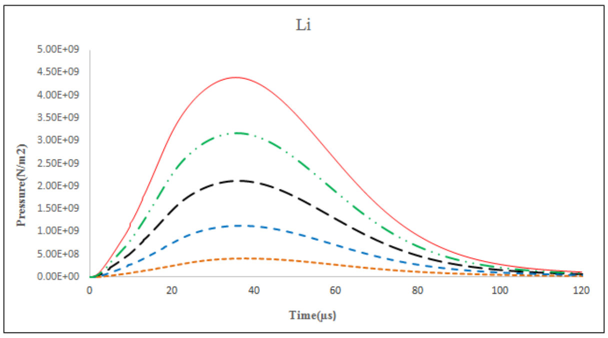

Figure 2. Plasma pressure of lithium at the capillary exit

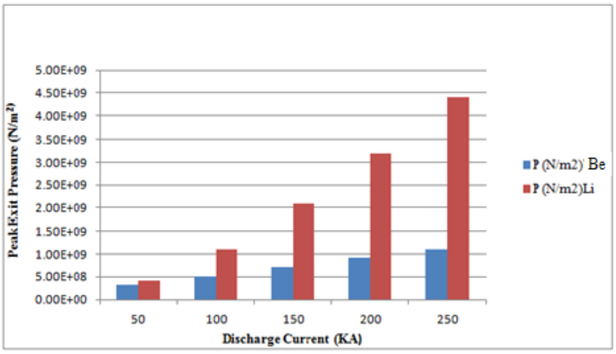

Figure 3. Comparison between Be and Li exit pressure at peak discharge currents

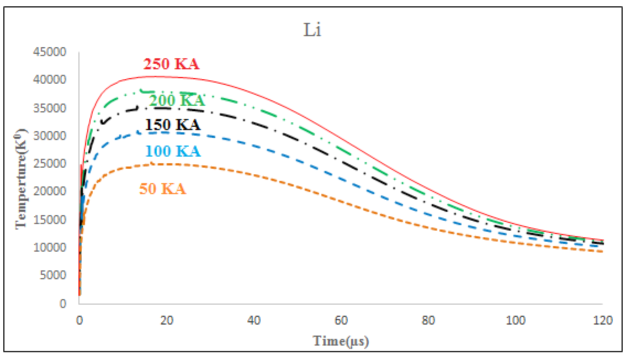

Figure 4. Plasma temperature versus time at the capillary exit for Li with currents up to 250 kA

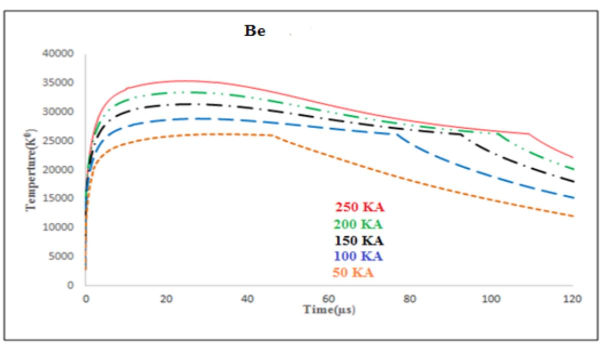

Figure 5. Plasma temperature versus time at the capillary exit for Be with currents up to 250 kA

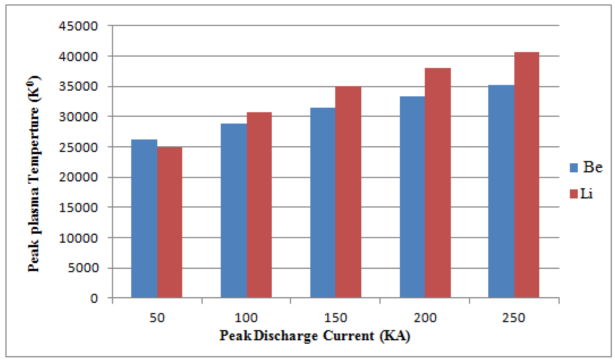

Figure 6. Comparison between plasma temperature for Be and Li at different peak currents

Figure 6 shows peak plasma temperatures of Li and Be with the peak of the discharge current. It is noticed that the temperature of Be is greater than that of Li at 50 kA discharge current, which agrees with the ideal behavior. However, the non-ideal behavior starts to appear at 100 kA current where the temperature of Li is becoming greater than that of beryllium.

The heat flux drops to a minimum for all discharge currents at the end of the discharge time, as shown in Figure 7 for Be and Figure 8 for Li, with values between 6.2-7.2 GW/m^2 for 50-250 kA, respectively.

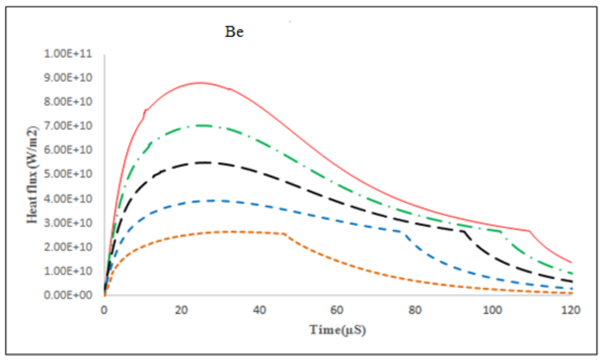

Figure 7. Heat flux versus time at the capillary exit when using Be as the liner

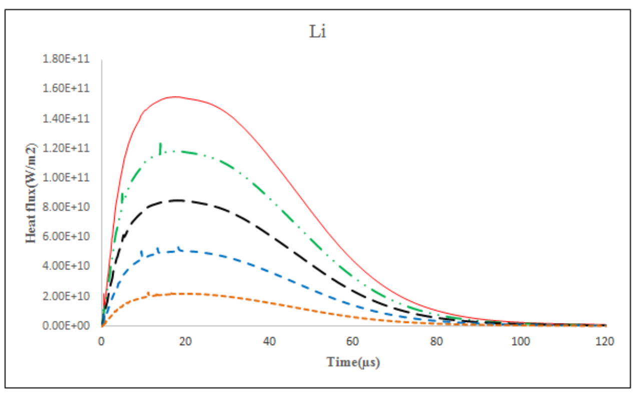

Figure 8. Heat flux versus time at the capillary exit when using Li as the liner

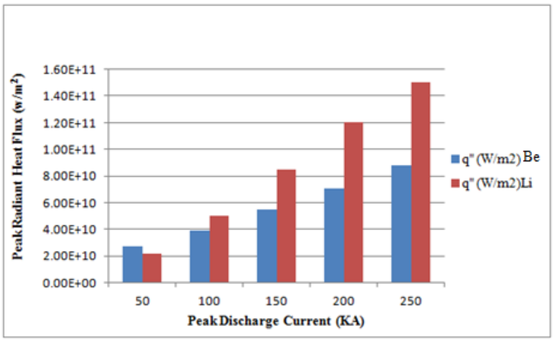

Figure 9. Heat flux versus peak current Li and Be at the capillary exit

Figure 9 shows the increase in the peak heat flux of Li and Be with the increase of the discharge current. Lithium shows increase in the heat flux more than Be except at 50 kA current where the heat flux of Be is greater than that of Li, which in turn affects the total ablated mass as shown in Figure 10.

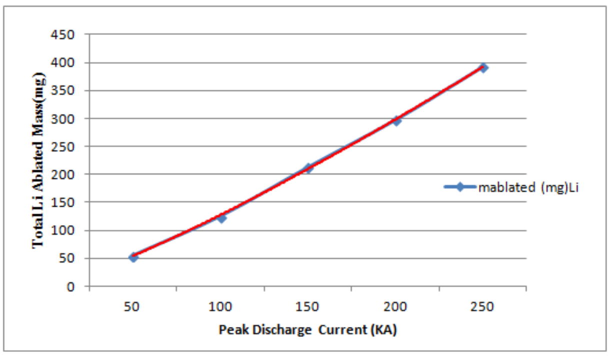

Figure 10. total ablated mass of Li versus peak discharge current

Figure 10 shows the total Li ablated mass released from the capillary for current values between 50 to 250 kA. Total ablation for 50 kA is 55 mg and increases to 392 mg for 250 kA. The power law is shown to be the best fitting with respect to the discharge current ($m_{Li\ total\ ablated(mg)} = 5.47\, I_{peak(kA)}^{1.22}$) and agrees with the general scaling of plasma parameters [17].

Mass ablation inside the source does not include any re-deposition or re-solidification and the total ablated mass is removed out of the capillary by the axial flow and the pressure effect.

Figure 11 shows the total Be ablated mass released from the capillary for current values between 50 to 250 kA. Total ablation for 60.8 kA is 55 mg and increases to 225 mg for 250 kA. A fit in a power law is preferable ($m_{Be\ total\ ablated(mg)} = 61.131\, I_{peak(kA)}^{0.815}$) and is also correlating well to the general scaling of plasma parameters [17].

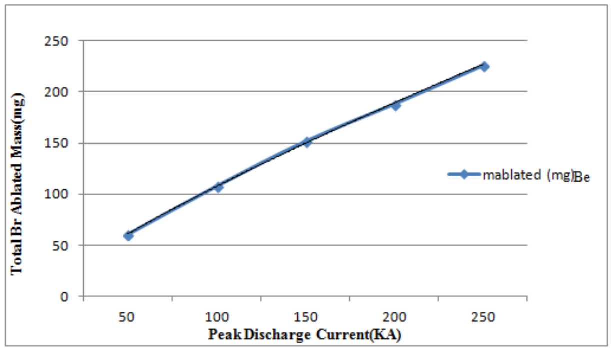

Figure 11. Beryllium total ablated mass versus peak discharge current

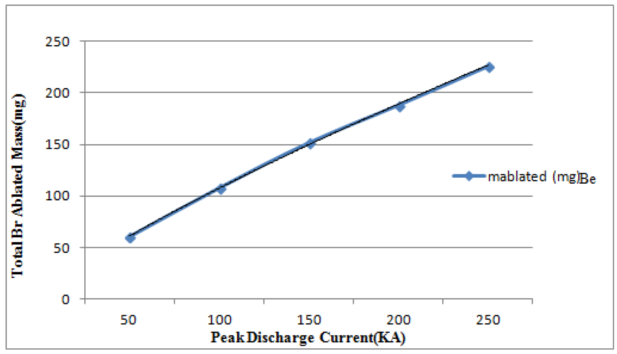

Figure 12. Total ablation of Li and Be versus peak discharge current

Figure 12 illustrates the total ablated mass of Be and Li versus the peak discharge current. It is noticed that at 50 kA current the beryllium has the highest ablation, while lithium is the lowest which agrees with the results of J. R. Echols and A. L. Winfrey where the plasma is in ideal regime [5]. While the non ideal plasma regime is more clear at higher discharge currents of 100 kA, 150 kA, 200 kA and 250 kA. Figure 13 shows the second and third ionization number densities of Be and Li versus peak discharge current, indicating initiation of third ionization when the discharge current exceeds150 kA. The increase in third ionization species provides contamination inside the core of plasma in fusion reactors. Lithium generates third ionized species much higher than Be, especially at high currents but they recombine more rapidly.

Figure 14 shows the peak number densities of all lithium plasma constituents, electrons, ions (first, second and third ionizations), neutrals and the total number density. The lines of electron number density and the number density of first ionization are nearly congruent because the most of electrons comes from the first ionization, the total number densities from second and third ionization are small relative to the number density of the first ionization. As noticed while the pulse length is increased, the number density of individual particles stays constant (which is expected due to the balance between the ionization and recombination rates) except the second and third ionization which increase for the first 25 μs then drops more rapidly near the end of the discharge period as a result of the recombination processes. The life time of third ionization is almost half the life time of second ionization.

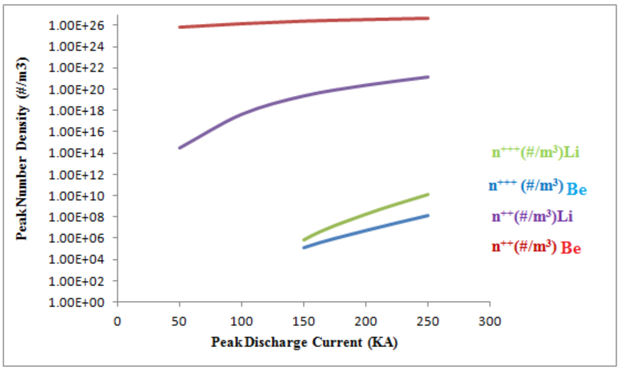

Figure 13. Second and third ionization number densities of Be and Li versus peak discharge current

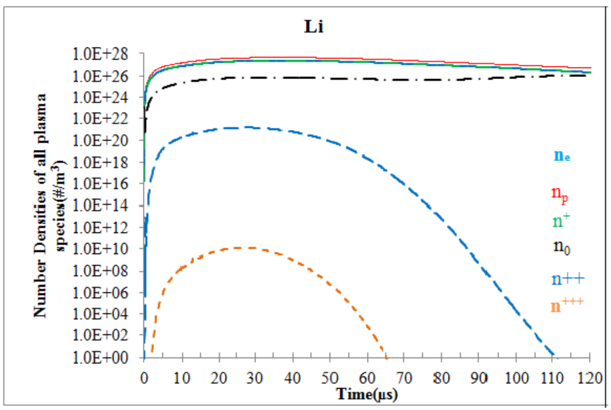

Figure 14. Number density of lithium ions compared to the total number density and the density of electrons

Figure 15 shows the peak number densities of all beryllium plasma constituents, electrons, ions (first, second and third ionizations), neutrals and the total number density. On contradiction with Li behavior, the number density of second ionization of Be stays unchanged with the increase of the pulse length as other individual particles, however the third ionization increases for the first 30 μs then slowly decays towards the end of the discharge period. The third ionization of Be is more consistent than the third ionization of Li which disappears completely at 65 μs.

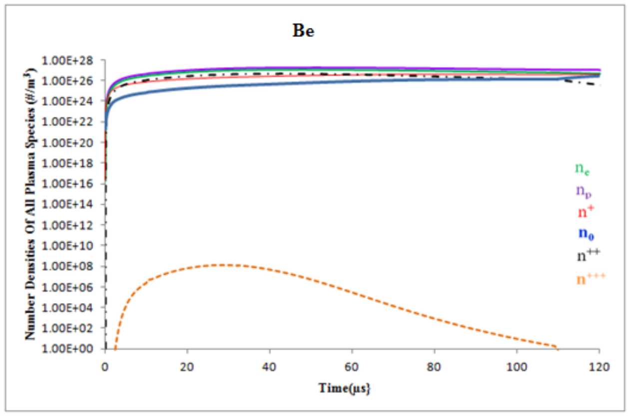

Figure 15. Number density of beryllium ions compared to the total number density and the density of electrons

Figure 16 shows the peak plasma-bulk velocities of Li and Be at the capillary exit versus the peak discharge current. As shown in the figure Li has the highest values of velocities which reaches 9000 m/s at 250 kA while the maximum velocity of Be at 250 kA is about 6500 m/s so many researchers used Li as pellet injection like the work of J. L. Terry et al. where they used injection of high-speed Li pellets to measure the internal magnetic field pitch on TFTR [18].

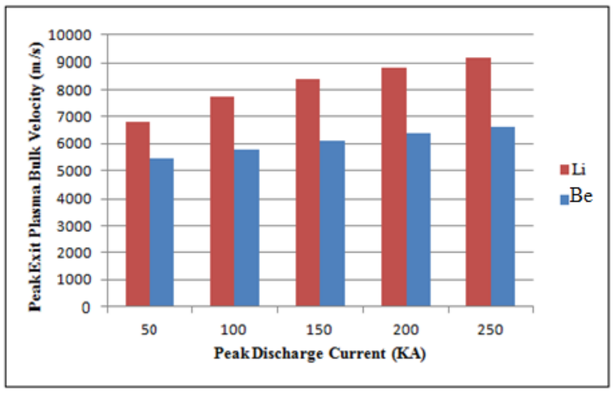

Figure 16. comparison between peak plasma bulk velocity at different peak discharge currents

Figure 17 shows the time evolution of the plasma bulk velocity at the last node (the capillary exit) for the 50 and 250 kA discharge currents. At the initiation of the plasma formation, the velocity rises sharply to reach its peak at the peak of the discharge current. The higher current has faster rise as compared to lower current values as shown in the figure. The velocity decreases with the decrease in the magnitude of the discharge current and drops from its peak of 5077 m/s for 50 kA to 2964 m/s at the end of the discharge at 120 μs. For the higher discharge current of 250 kA, the bulk velocity drops from its peak value of 6507 m/s to 3811 m/s at 120μs. It concludes that the exit velocity at the end of the discharge cycle is in the range of 2900-3800 m/s for currents between 50 to 250 kA. Similar behavior can be seen in Figure 18 when beryllium is the liner material in the capillary.

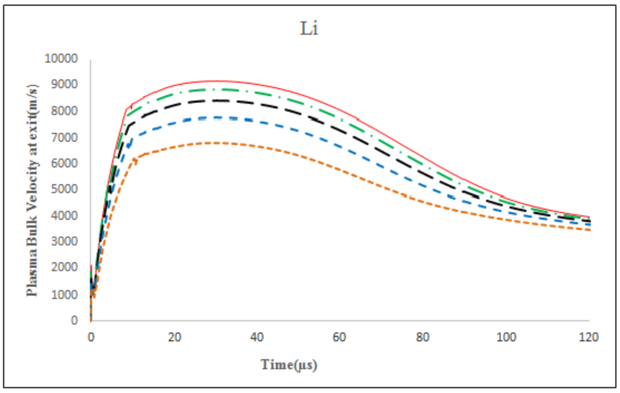

Figure 17. Plasma bulk velocity at source exit for lithium liner in the capillary

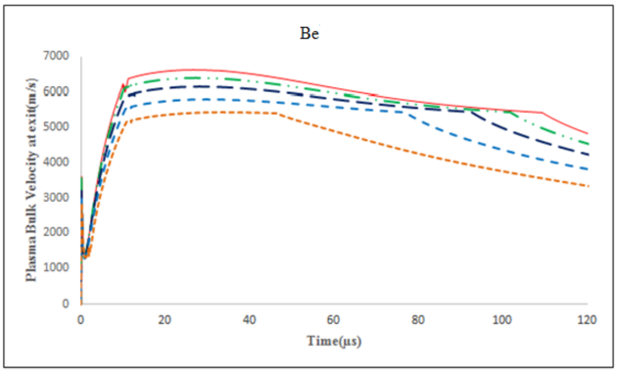

Figure 18. Plasma bulk velocity at source exit for beryllium liner in the capillary

4. Conclusions

A detailed study was performed to compare between Beryllium and Lithium as fusion materials for plasma-facing components in future fusion reactors. Computational experiments using ETFLOW code were conducted. Beryllium and lithium demonstrate lower ablation rates at all levels of tested heat fluxes between 10 and 125 GW/m^2, however the ablation rates increase sharply from 125 GW/m^2 and 288GW/m^2, especially Li which shows double ablation rates more than Be. Both Li and Be have a specific merits which nominate each of them to a fixed function inside the reactor that related to design, engineering, and operation are rather closely matched. The generation of third ionization is a particular behavior regarding using peak discharge currents of 50-250 kA, which produces heat fluxes from 57 to 288 GW/m^2. The generation of third ionization starts obviously from 150 kA for both element and Li^{+++} shows a small increasing than Be^{+++} by two orders of magnitude at 250 kA. Plasma temperature varies from 25000 K for both elements to 35000 for Be and 40000 for Li at the lowest and highest heat fluxes, respectively. The high exit velocity of Li which arrives at 9000m/s nominates it to be used as a high-speed pellet injector inside the reactors for deep fueling. The generation of Be^{++}which is nearly equals Be^{+} is staying unchanged and does not suffer any recombination for a long time. Achieving higher ionizations in such high-density plasmas turns the plasma to behave weakly nonideal and hence the conductivity model of the non-ideal plasma was employed.

References

[1] Robert, W.C., Russell, P. Doerner, Jongik Won, 1997. Beryllium as the plasma-facing material in fusion energysystems—experiments, evaluation, and comparison with alternative materials, Fusion Engineering and Design. 37, 481-513.

[2] Asif, M., 2014. The HT-7 Team, Theoretical Calculation of Effective Ionic Charge with Lithium Limiter on HT-7 Tokamak, J Fusion Energ. 33, 444-448.

[3] Hassanein, A., Ehst., D.A., 1994. Beryllium and graphite performance in ITER during a disruption , Journal of Nuclear Materials. 212-215, 1272-1277.

[4] Federici, G., Skinner, C.H., Brooks, J.N., Coad, J.P., Grisolia, C., Haasz, A.A., Hassanein, A., Philipps, V., Pitcher, C.S., Roth, J., et al., 2001. Plasma-material interactions in current tokamaks and their implications for next step fusion, reactors Nuclear Fusion. Vol. 41, No. 12R.

[5] Echols, J.R., Winfrey, A.L., 2014. Ablation of Fusion Materials Exposed to High Heat Flux in an Electrothermal Plasma Discharge as a Simulation for Hard Disruption, J Fusion Energ. 33, 60-67. DOI: https://doi.org/10.1007/s10894-013-9639-4.

[6] Barabash, V., Eaton, R., Hirai, T., Kupriyanov, I., Nikolaev, G., Wang, Zh.H., Liu, X., Roedig, M., Linke, J., 2011. Summary of beryllium qualification activity for ITER first-wall applications, Phys. Scr. T145, 014007.

[7] Snipes, J.A., 1992. Wall conditioning with impurity pellet injection on TFTR, Journa of nuclear materials. 196-198, 686-691.

[8] Majeski, R., Jardin, S., Kaita, R., Gray, T., Marfuta, P., Spaleta, J., Timberlake, J., Zakharov, L.E., Ghassan Antar, R., Doerner et al., 2005. Nucl. Fusion. 45, 519-523.

[9] Mirnov, S.V., Azizov, E.A., Evtikhin, V.A., Lazarev, V.B., Lyublinski, I.E., Vertkov, A.V., Yu Prokhorov,

D., 2006. Plasma Phys. Control. Fusion 48, 821.

[10] Apicella, M.L., Lazarev, V., Lyublinski, I., Mazzitelli, G., Mirnov, S., Vertkov, A., 2009. Lithium capillary porous system behavior as PFM in FTU tokamak experiments. Journal of Nuclear Materials. 386-388, 821-823.

[11] Evtikhin, V.A., Lyublinski, I.E., Vertkov, A.V., Azizov, E.A., Mirnov, S.V., Lazarev, V.B., Sotnikov, S.M., Safronov, V.M., Prokhorov, A.S., Korzhavin, V.M., June 2004. Main Directions and Recent Test Modeling Results of Lithium Capillary-Pore Systems as Plasma Facing Components, Plasma Science & Technology. vo1.6, No.3.

[12] Hu, J.S., Zuo, G.Z., Li, J.G., Luo, N.C., Zakharov, L.E., Zhang, L., Zhang, W., Xu, P., 2010. Investigation of lithium as plasma facing materials on HT-7, J.S. Hu et al. / Fusion Engineering and Design. 85, 930-934.

[13] Ruzic, D.N., Shaheen, M., 1992. Wall conditioning with impurity pellet on TFTR, Journal of nuclear materials. 196-198, 686-691.

[14] Spitzer, L., Härm, R., Mar. 1953. Transport phenomena in a completely ionized gas. Phys. Rev. 89(5), 971-981.

[15] Zaghloul, M.R., Bourham, M.A., Doster, J.M., Powell, J.D., October 1999. On the Average Electron-Ion Momentum Transport Cross-Section in Ideal and Nonideal Plasmas. Physics Letters A. Vol. 262/1, pp. 86-89.

[16] Zaghloul, M.R., Bourham, M.A., Doster, J.M., April 2000. Energy-Averaged Electron-Ion Momentum Transport Cross-Section in the Born Approximation and Debye-Huckel Potential: Comparison with the Cut-Off Theory. Physics Letters A. Vol. 268/4-6, pp.375-381.

[17] Vergara, P.P., Gilligan, J., Winfrey, L., Bourham, M., 2015. Generalized Scaling Laws of Plasma Parameters in Electrothermal Plasma Sources for Fusion Disruption Erosion and Hypervelocity Launch Applications, IEEE Trans Plasma Sc. 43(10), 3645-3652 .

[18] Terry, J.L., Marmar, E.S., Howell, R.B., 1990. Measurement of internal magnetic field pitch using Li pellet injection on TFTR (invited), Review of Scientific Instruments. 61, 2908.
DOI: https://doi.org/10.1063/1.1141775.

New Energy Exploitation and Application
http://ojs.ukscip.com/index.php/NEEA/issue/view/2

RESEARCH ARTICLE

The Thermohydraulic Characteristics Investigation of the Aluminum Alloy Monometallic Plate-finned Tube in Together with Numerical Simulation of Heat and Mass Transfer Processes

Sergey V. Tiunov[1] Ruslan M. Nizamutdinov[2*] Ilmir I. Khabibullin[2]

1. Termocam LLC, Kamsky Polyani, Tatarstan, 423564, Russia
2. Kazan, Tatarstan, 420029, Russia

Received: 28 December 2021; **Accepted:** 23 January 2022; **Published Online:** 26 January 2022

Abstract: The article is devoted to the investigation of aluminium alloy plate-finned tube characteristics regarding the heat exchange intensification. Outer thick finning, inner ribs quantity and rib shape allow to increase heat exchange efficiency. However, the most important task is finding an optimal combination of pipe geometry parameters. Seven different ribbed tube samples were investigated during the experiment. The samples differed by geometry, quality and quantity of ribbing, and consequently hydraulic and thermodynamic characteristics. The main criteria for an integrated assessment of pressure losses and energy indicators were the criteria of Kirpichev and Antufiev. The above evaluation criteria were intended for an overall assessment of sample effectiveness based on experimental data. In advance and parallel with a natural experiment, a numerical experiment was conducted. The purpose of the numerical experiment was obtaining an adequate model of the heat exchange section to be used in a full-sized oil cooler model in the future. Thus, the article discusses the results of comparing natural and numerical investigations and the prospect of using the best sample in the oil cooler composition. The ultimate goal is the development of an automatic air-cooling apparatus with a compact high-performance oil cooler.

Keywords: Plate-finned tube, Heat exchange section, Oil cooler, Air-cooled heat exchanger, Air-to-oil heat exchanger, Intensifier, Outer fin, Inner rib, Fin pitch, Rib height, Channel wall thickness, Tube width, Tube height; Inner channel quantity, Full-scale experiment, Numerical investigation, Thermal power, Thermal efficiency

1. Introduction

Air-cooled heat exchangers are used in different domains, including nuclear, aviation, chemical, oil and gas extracting industries. Despite the fact that a heat exchanger is a part of support equipment, its role in operation of primary equipment is extremely significant.

The key and characteristic element of any oil cooler is the cooling (or heat exchange) section, which can consist of smooth or finned tubes that intensify heat transfer. This is well known that the heat exchange intensifier usage [1]

*Corresponding Author:
Ruslan M. Nizamutdinov,
Kazan, Tatarstan, 420029, Russia;
Email: ruslan.nizamutdinov@niitk.ru

DOI: https://doi.org/10.54963/neea.v1i1.23

is the best way to decrease overall size, increase energy efficiency and reduce the cost of heat exchange apparatus, in the whole. The most spread rib types are represented in Figure 1 [1-4].

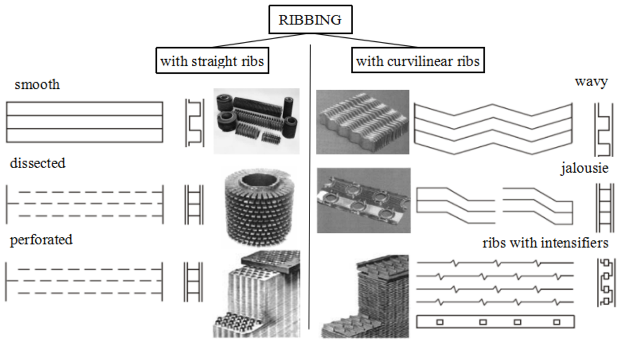

Figure 1. Types of ribbing

This study represents some results of natural and numerical investigations of lamellar-ribbed tube samples. The samples are made of aluminium alloy and in fact, they are varieties of monometallic tubes with dissected ribbing (Figure 2). According to study [6], the heat transfer coefficient of a dissected (serrated) finned tube is 20 percent more than smooth finned tube. Low transitional thermal resistance and high thermal conductivity in combination with cheap manufacturing make the aluminum alloy monometallic flat tube usage preferable in comparison with a steel round spiral-finned tube.

The objective of this study is a trial and subsequent analysis of quantitative thermohydraulic characteristics of the lamellar-ribbed monometallic aluminium alloy flat tube obtained during natural and numerical experiments. The most effective design could be applied in an automatic air-cooled heat exchanger.

2. Materials and Methods

Experimental Investigation

Firstly, some results of the experimental research of air-to-oil heat exchanger elements are viewed. The element (a monometallic tube) with developed heat exchange surface made of aluminium alloy is shown in Figure 2.

The crosscuts of the cooling section with six inner channels are shown in Figures 3. The tube has a rectangular profile with inner channels (Figure 3a) produced with mechanical tools. There are specially formed fins on the outer surface providing the intense heat transfer with air. The longitudinal solid edges in the inner rectangular channels have oil side mass and heat transfer intensifiers (Figure 3b, 3c).

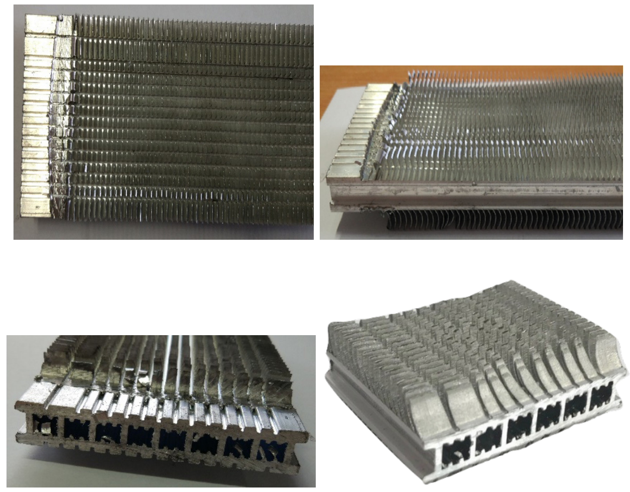

Figure 2. Monometallic tube (cooling section) samples

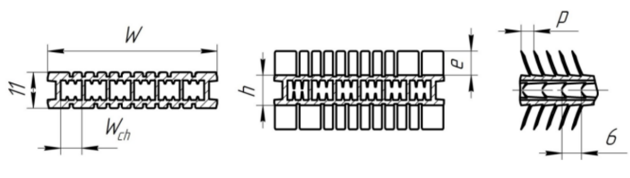

a) b) c)

Figure 3. The cooling section [5]: a) tube profile; b), c) cooling section profile

Figure 4 illustrates a scheme of the test rig, which was used to get the quantitative heat and hydrodynamic characteristics of the cooling section during the research.

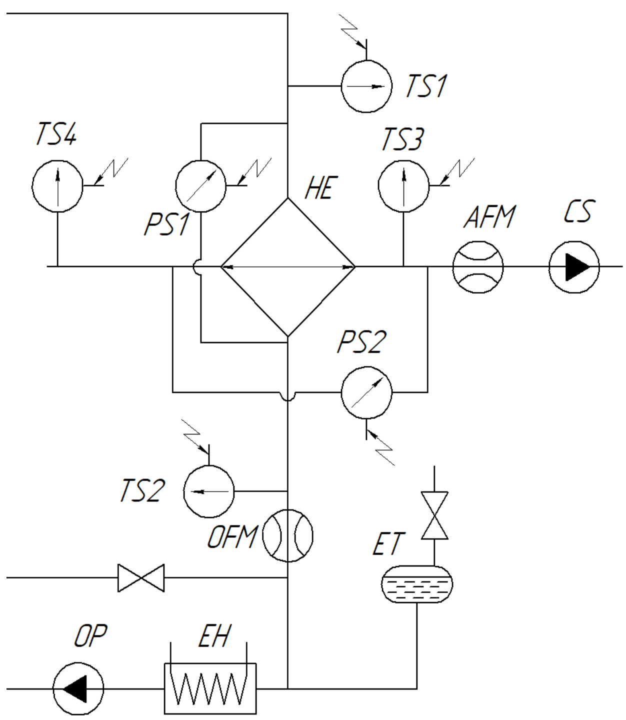

Figure 4. Test rig scheme

The scheme includes: a characteristic element (a single cooling air-to-oil heat exchanger section) HE; an oil pump OP; an oil electric heater EH; an oil ultrasonic flow meter OFM; an expansion tank ET; oil temperature sensors TS1-TS2; differential pressure sensors PS1-PS2; an air centrifugal supercharger CS; an air flow meter AFM; air temperature sensors TS3-TS4. Measuring means list is represented in Table 1.

Table 1. The measuring means list

Name, type and marking	Quantity	Standard, Specification or designation
Sixteen channel stationary air velocity meter	1	TTM-2/16-06-8P-8A by «EKSYS» firm
Thermo anemometer	11	TTM-2-04-01 by«EKSYS» firm
Power supply	1	TPM138
Pressure sensor	1	AIR 20/M2-DD
Pressure sensor	1	OVEN PD200
Pump, heater	1	PFM1-4
Ultrasonic flow meter	1	PortoFlow330
Temperature sensor	4	Pt-100
Centrifugal supercharger	1	VR 132-30-8

PFM1-4 unit (5 kW power and 4 m^3/hr capacity) was implemented into the test rig to pump and heat coolant. VR 132-30-8 centrifugal supercharger (15 kW power at 1500 rpm) was used for cooling air feeding. OVEN PCHV 204-15K-V frequency control device, realized adjustment of centrifugal supercharger frequency. Working fluid was TP-22C oil (technical specification TU 38.101821-2013).

Special connecting pipes with seats for pressure and temperature sensors were designed and printed with 3D printer to provide the uniform oil flow rate in the heat exchanger channels, shown in Figure 5.

Figure 5. The connecting pipe

Table 2. Defined parameters and their measurement accuracy

No	Parameter name	Measure unit	Measurement limit deviations
1.	Oil heat exchanger inlet temperature	ºC	2%
2.	Oil heat exchanger outlet temperature	ºC	2%
3.	Air heat exchanger input temperature	ºC	2%
4.	Air heat exchanger output temperature	ºC	2%
5.	Oil flow meter indication	litre/minute	1%
6.	Air velocity indication in the channel	m/s	3%
7.	Air velocity before cooling section	m/s	3%
8.	Air velocity after cooling section	m/s	3%
9.	Air temperature after cooling section	ºC	3%
10.	Air temperature before cooling section	ºC	3%
11.	Air drop pressure	Pa	±3%
12.	Oil drop pressure	Pa	±3%

Instruments and experiment technique are described below the passage. The oil temperature at the heat exchanger inlet and outlet was measured with PT100 resistance thermometers and RMT-59 register to determine the heat flow. The oil flow value was determined with Porto Flow 330 ultra-sonic flow meter. Simultaneously, the heat flow determination in the second (air) contour was performed by measurement of input and output temperatures and the air flow rate value. Table 2 represents the list of defined parameters and their measurement accuracy.

Seven samples of monometallic tube were investigated during the research. Table 3 represents the basic geometric parameters of the test samples.

Table 3. Geometrical characteristics of monometallic tube samples (Figure 3)

Sample No	Fin pitch *p*, [mm]	Fin height e, [mm]	Channel wall thickness of the tube, [mm]	Tube width W, [mm]	Tube height h, [mm]	Inner channel quantity, pcs	Inner channel width W_{ch}, [mm]
1	2	8.5	1.2	52	8.0	6	6
2	2	6,5	1.2	52	8.5	6	6
3	2,5	4	1.2	52	8.5	6	6
4	3.75	5.5	1.2	52	8.5	6	6
5	2.5	8	1.2	67.5	8.3	8	6
6	2.5	8	1.2	67.5	8.5	8	6
7	3.75	6	1.2	67.5	9.2	8	6

he experimental results were processed according to the following equations [2].

Heat capacity:

$$Q = c_p \cdot G \cdot \Delta T_{max}, \quad (1)$$

where Q is the heat capacity of the cooling section, W;

c_p-the specific heat capacity at the constant pressure, J/(kg·K);

G-the coolant mass flow, kg/s;

ΔT_{max}-the maximal temperature deference of the coolant at the input and the output, °C.

The total thermal resistance to heat transfer:

$$R = 1/k, \tag{2}$$

where k is the heat transfer coefficient, (m^2 K)/W, determined by formula

$$k = Q/(F \cdot \overline{\Delta t}), \tag{3}$$

where F is the outer surface heat transfer area without accounting of fins, m^2, determined by formula

$$F = 2 \cdot (W + h) \cdot L, \tag{4}$$

where $\overline{\Delta t}$ is the average logarithmic temperature head of the cooling section at the transverse flow.

The next parameter is a compactness factor, m^2/m^3, determined by formula

$$k_{CP} = F/V, \tag{5}$$

where F is the surface heat transfer area, m^2, of any coolant side to the cooler core (matrix) volume, m^3.

The cooling section thermal efficiency was calculated by the next formula

$$\eta = Q/Q_{max}, \tag{6}$$

where Q is the heat capacity and Q_{max} is the highest possible heat capacity, W, of the cooling section.

3. Results

Measurement data processing results for seven samples are represented in Table 4.

After processing measurement results, thermal power on mode parameters graphical dependencies were obtained for every sample, Figure 6.

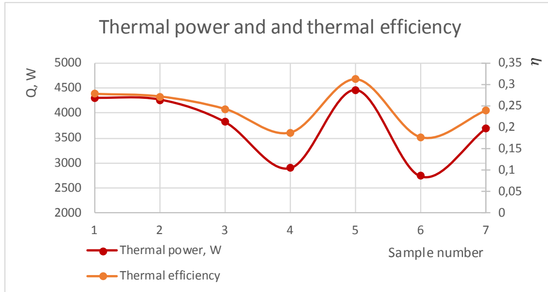

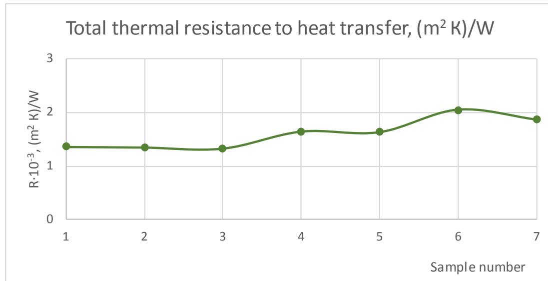

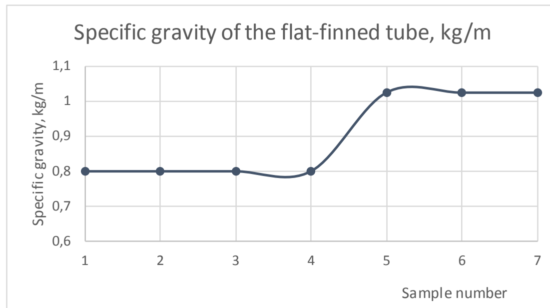

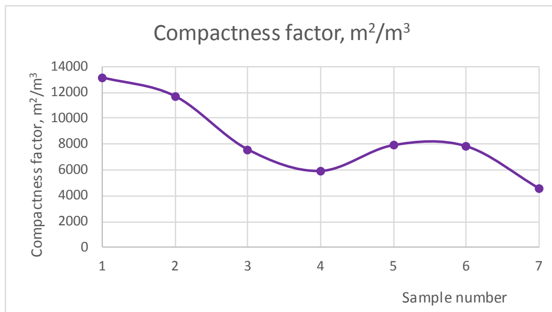

Table 4. Thermal characteristics of monometallic tube samples

Sample No	Thermal power, W	Thermal efficiency	Total thermal resistance to heat transfer, (m^2 K)/W	Specific gravity of the flat-finned tube*, kg/m	Compactness factor, m^2/m^3
1	4302	0,278	$1,36 \cdot 10^{-3}$	0,802	13156
2	4267	0,272	$1,35 \cdot 10^{-3}$	0,802	11720
3	3821	0,243	$1,33 \cdot 10^{-3}$	0,802	7580
4	2905	0,188	$1,64 \cdot 10^{-3}$	0,802	5888
5	4457	0,312	$1,63 \cdot 10^{-3}$	1,025	7885
6	2738	0,177	$2,04 \cdot 10^{-3}$	1,025	7821
7	3700	0,24	$1,86 \cdot 10^{-3}$	1,025	4566

* the monometallic flat-finned tube one meter weight

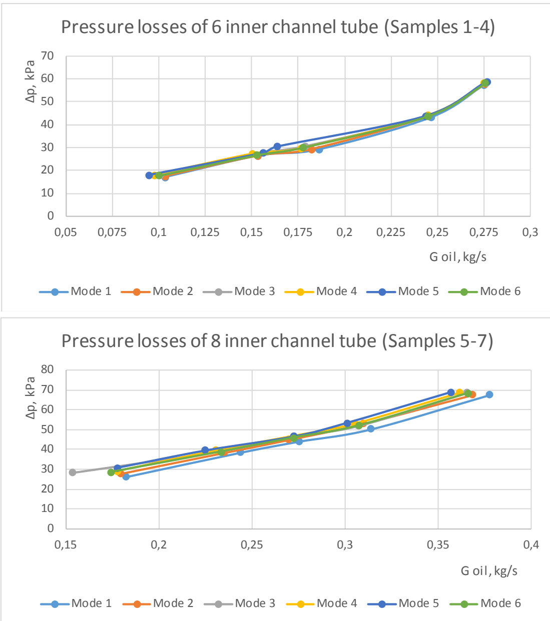

Figure 6. Graphical dependencies of measurement data processing results for seven samples

Figures 7 illustrates thermal power dependencies on oil-side Reynolds numbers at fixed air-side Reynolds numbers for samples 2 and 5 respectively.

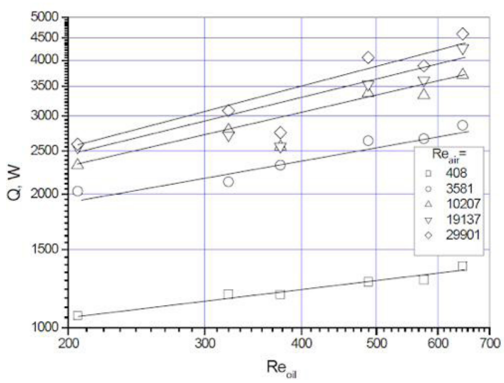

a) sample 2

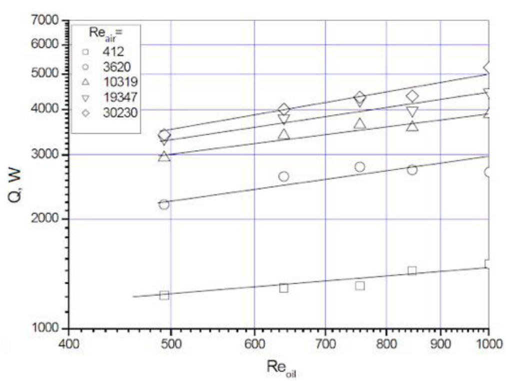

b) sample 5

Figure 7. Thermal power on mode parameters graphical dependencies for samples 2 and 5

Figure 8 shows the comparison of test samples by Kirpichev energy efficiency criterion-E [9], which is determined by formula

$$E = Q/N, \tag{7}$$

where Q is the heat capacity, W, see formula (1),

N-the pumping power of oil and/or air, W, which is determined by formula

$$N = G\cdot\Delta P/(\rho\cdot\eta), \tag{8}$$

where G-the oil/air mass flow, kg/s,

ΔP-oil/air side pressure losses, Pa,

ρ-oil/air density, kg/m^3,

η-the efficiency factor of a pump or ventilator.

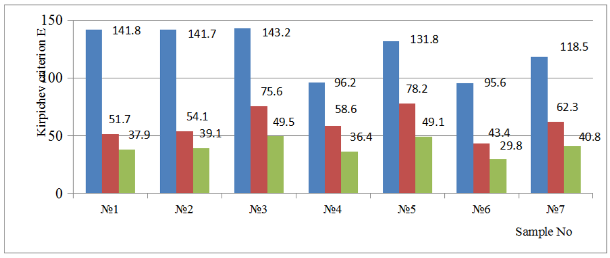

Figure 8. Kirpichev energy efficiency criterion (E) of test samples: N_{air} calculation, N_{oil} calculation, (N_{air} + N_{oil}) calculation.

Figure 9 illustrates the graphical comparison of test samples by Antufiev energy efficiency criterion [10] determined by formula

$$E^{'} = \dot{Q}/(N\cdot\overline{\Delta t}), \tag{9}$$

where Q is the heat capacity, W, formula (1),

N is the pumping power of oil and/or air, W, formula (8),

$\overline{\Delta t}$ is the average logarithmic temperature head of the cooling section at the transverse flow.

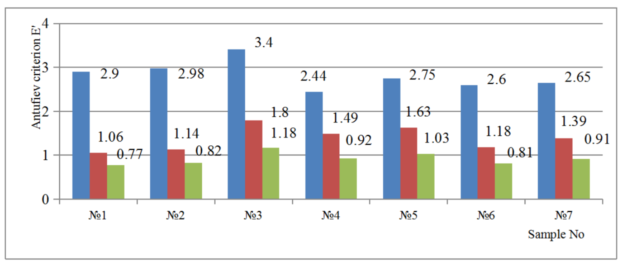

Figure 9. Antufiev energy efficiency criterion () of test samples: N_{air} calculation, N_{oil} calculation, (N_{air} + N_{oil}) calculation.

Numerical investigation

Numerical modeling was undertaken to obtain an adequate model of the heat exchange section, in order to subsequently create full-sized models, firstly, of oil cooler and, secondly, automatic air-to-oil heat exchanger. Thus, obtaining the characteristic oil cooler element numerical model is the first step for further processes simulation of the full-sized apparatus. Process simulation was performed in the ANSYS® environment.

In view of the fact that the heat exchange (cooling) section is a flat-finned pipe of strict geometry with periodically repeating items (outer and inner fins, inner channels), the simulation methodology is based on the calculation of the heat exchange section element (shown in Figure 10) at average oil temperatures. Obtaining the general thermal and hydraulic characteristics of the whole section is done by multiplying by the corresponding amount of these elements along the cooling section. The regular element (Figure 10) is built with CAD tools and corresponds with the schemes shown in Figure 3 and photo in Figure 2. This is the first step in building a numerical model-geometric.

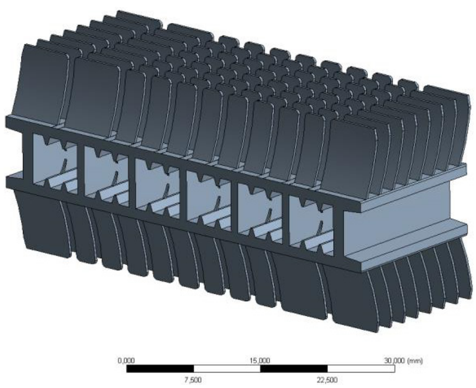

Figure 10. Regular element of the heat exchange section

The second step is creating air side and oil side working fluid domains. The domains are extended to simulate the heat cooling section before and after the regular element (see Figure 11).

At the third step, a finite element (FE) mesh is constructed for each domain. An ANSYS Meshing grid generator is used to create a FE-volume model of the computational grid. The calculated domain grids shown in Figures.

The FE mesh regular element model has 2945346 nodes, the air domain has 4244246 nodes, and the oil domain has 7967807 nodes. Prismatic sub-layers are constructed for the air and oil domain. The minimum cell size is 0.1 mm.

The boundary conditions at the inlet and outlet calculated area of the external air and oil circuits are velocity and pressure change terms, temperature and flow values, permeability coefficients, porosity coefficients, double cell model for simulating the heat transfer process between external air and oil circuits. The efficiency of the oil cooler is determined by the dependence on air and oil flow rates, according to nature experiments.

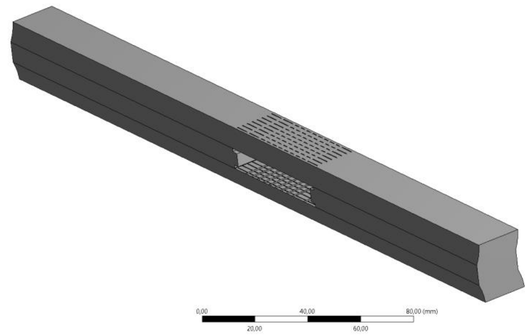

a) air carrier domain

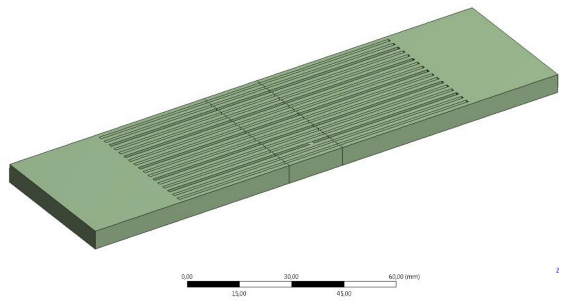

b) oil carrier domain

Figure 11. Working fluid domains

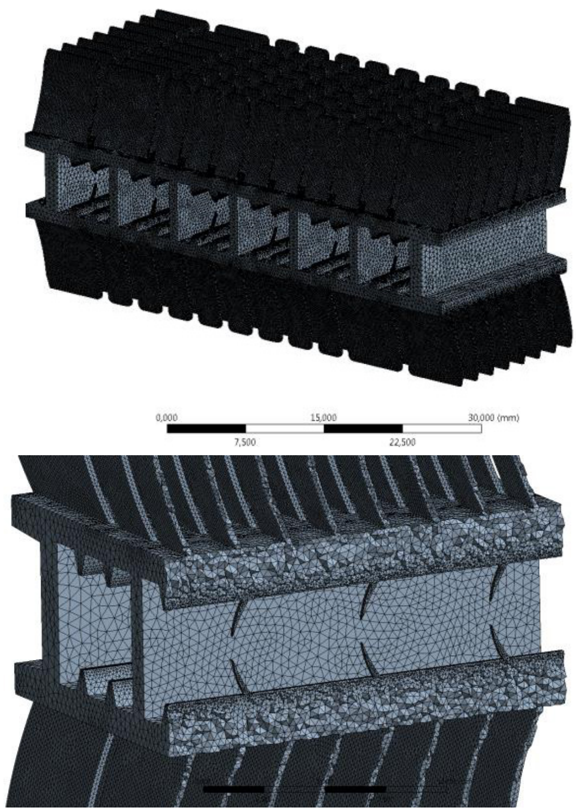

Figure 12. The regular item FE grid

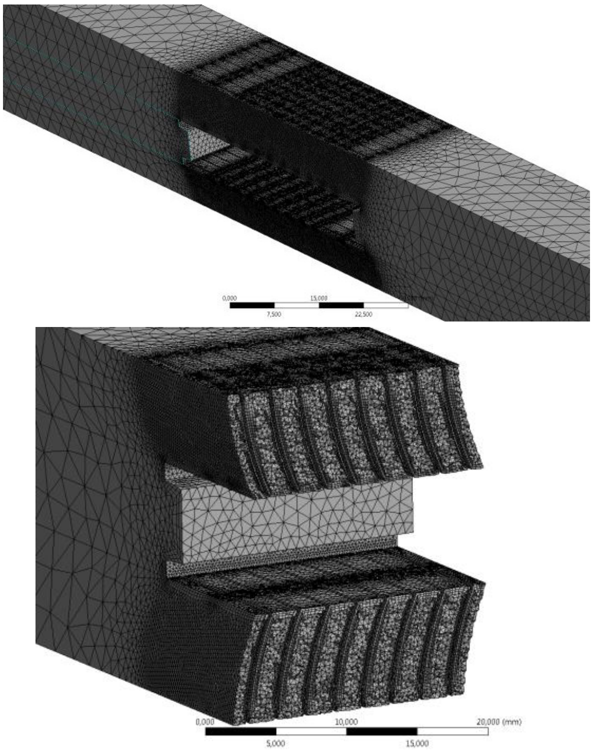

Figure 13. The air domain FE grid

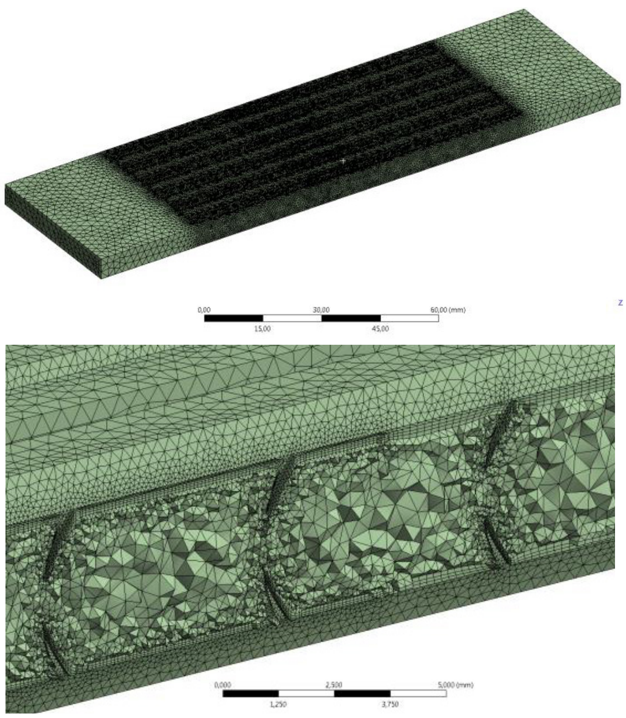

Figure 14. The oil domain FE grid

Then, the FE grids of the computational domains are transferred to CFX ANSYS®, where boundary conditions are assigned (Figure 15). The following boundary conditions are assigned for the regular item: air velocity at the element inlet 7.96 m/s, temperature 20 °C, mass oil flow through the element 0.148 kg/s, oil temperature 65 °C. The BSL model is used to calculate the task.

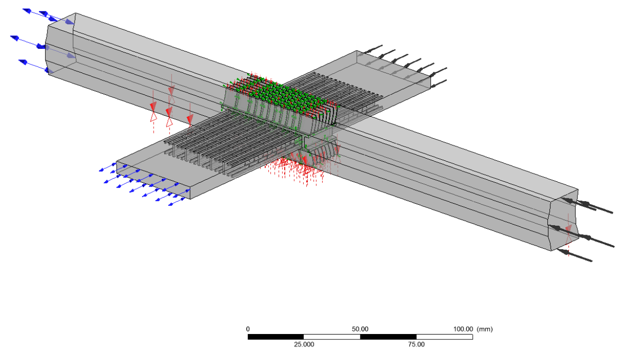

Figure 15. Boundary conditions

The calculation results of pressure, temperature, and velocity fields are presented in Figures 16-19. The air flow structure is shown in Figure 19b.

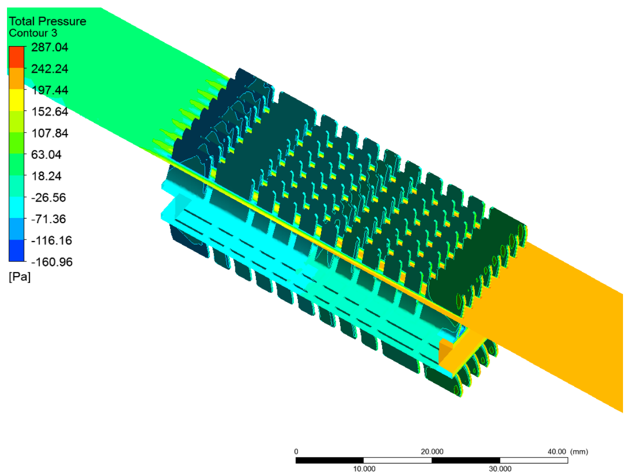

a)

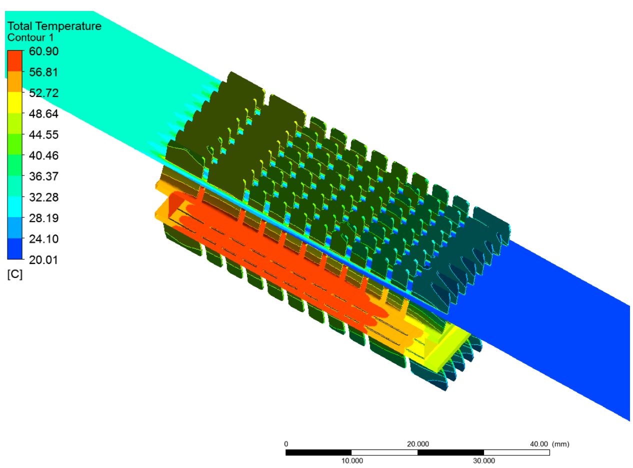

b)

Figure 16. Pressure (a) and temperature (b) fields in the air path

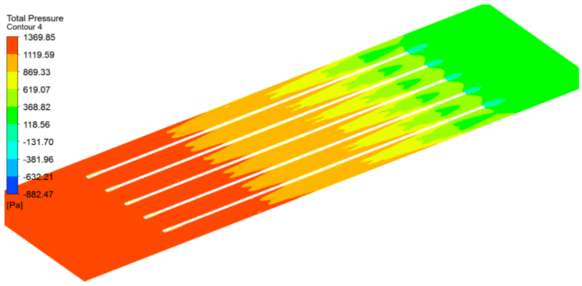

a)

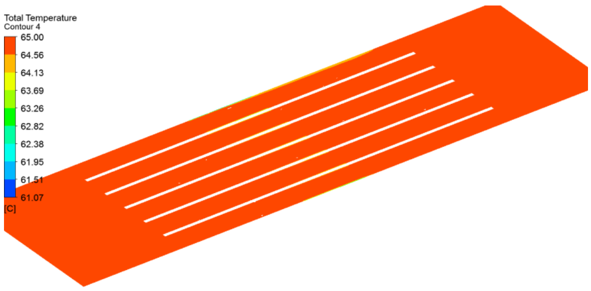

b)

Figure 17. Pressure (a) and temperature (b) fields in the oil path.

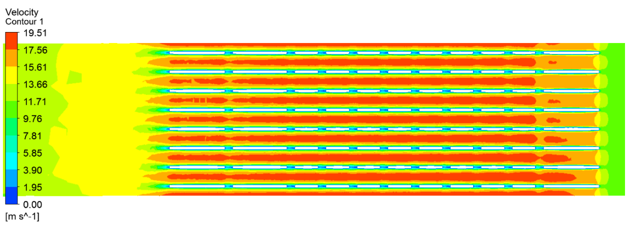

a)

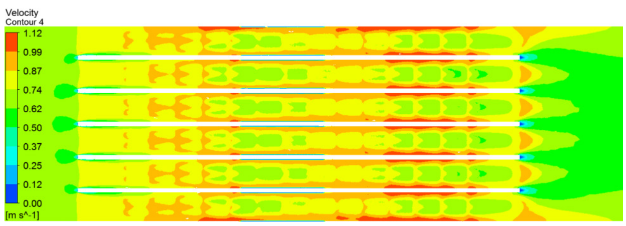

b)

Figure 18. Velocity fields in the air (a) and oil (b) path.

The numerical experiment results are summarized in Tables 5-9 and presented by graphical dependencies in Figures 20-22 below.

Table 9 summarizes the numerical study results of pressure losses in a single channel with and without ribs. The graph in Figure 22 clearly illustrates the difference in pressure loss values during oil flow in a finned and smooth channel.

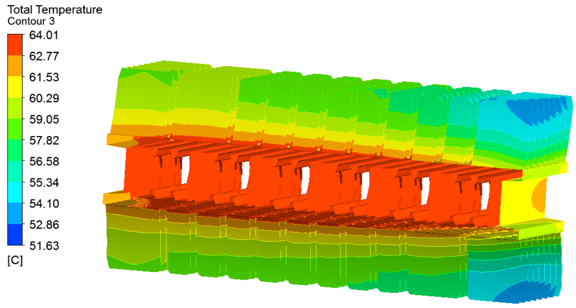

a)

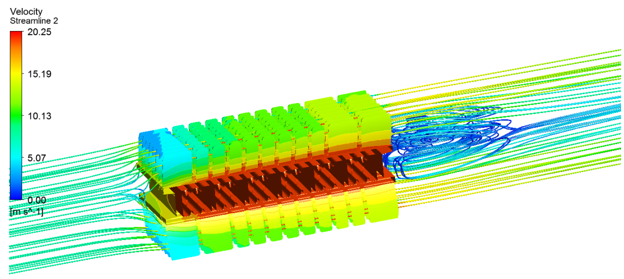

b)

Figure 19. Temperature fields on the internal and external interfaces (a) and air domain flow structure (b)

Table 5. Thermal power in dependency on air and oil mass flow rates

Air mass flow rate G_{air}, kg/s	Thermal power Q, W				
	Oil mass flow rate G_{oil}, kg/s				
	0,1791	0,2344	0,2738	0,3088	0,3669
0,0549	1234,07	1293,71	1310,09	1440,07	1502,95
0,1549	2189,97	2615,59	2779,16	2726,19	2683,97
0,2601	2943,05	3391,6	3630,68	3564,86	3878,94
0,3446	3320,4	3780,62	4230,5	3969,8	4457,31
0,4195	3406,98	3999,68	3314,26	4348,85	5210

Table 6. Thermal efficiency in dependency on air and oil mass flow rates

Air mass flow rate G_{air}, kg/s	Thermal efficiency η					
	Oil mass flow rate G_{oil}, kg/s	0,1791	0,2344	0,2738	0,3088	0,3669
	$c_{p\ air}/c_{p\ oil}$	362,497	474,2589	553,9499	624,8944	742,4873
0,0549	55,1328	0,5394	0,5654	0,5726	0,6294	0,6569
0,1549	156,9519	0,3362	0,4016	0,4267	0,4185	0,4121
0,2601	261,3817	0,2713	0,3127	0,3347	0,3286	0,3576
0,3446	346,9078	0,231	0,2631	0,2944	0,2762	0,3101
0,4195	421,5587	0,2265	0,2286	0,2466	0,2486	0,2978

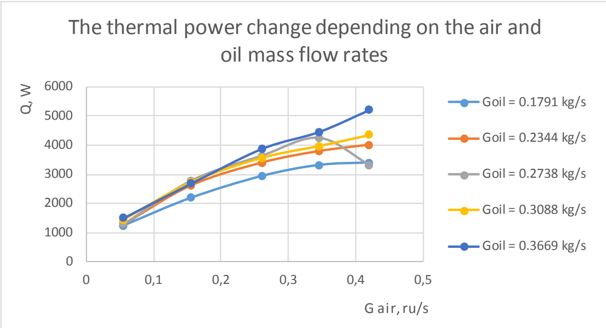

a)

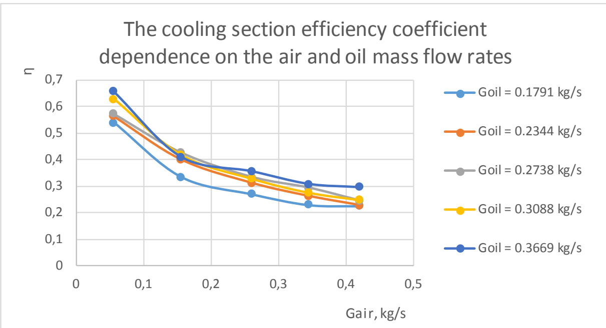

b)

Figure 20. Thermal power and efficiency graphical dependencies on air and oil mass flow rates (determined numerically)

Table 7. Air pressure losses in dependence on air velocity

Parameter	Value				
Air flow rate G air, kg/s	0,0549	0,1549	0,2601	0,3446	0,4195
Air velocity w air, m/s	1,0902	3,1036	5,1685	6,8479	8,3359
Air pressure losses Δp, Pa	8,97	47,2	104,7533	165,5333	256,5

Table 8. Oil pressure losses in dependence on oil velocity (mass flow rate of the whole section)

Parameter	Value				
Oil flow rate G oil, kg/s	0,1791	0,2344	0,2738	0,3088	0,3669
Oil velocity w air, m/s	0,1237	0,1619	0,1891	0,2133	0,2534
Oil pressure losses Δp, Pa	29166,66	39066,66	46633,33	51966,66	68200

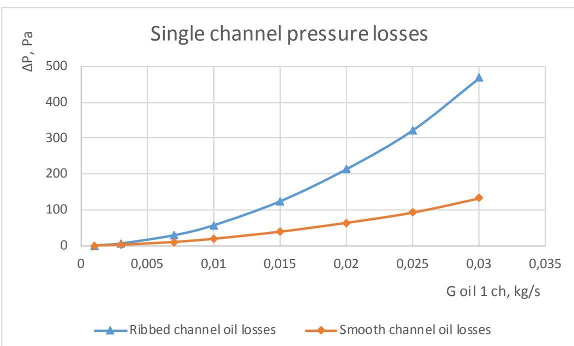

a)

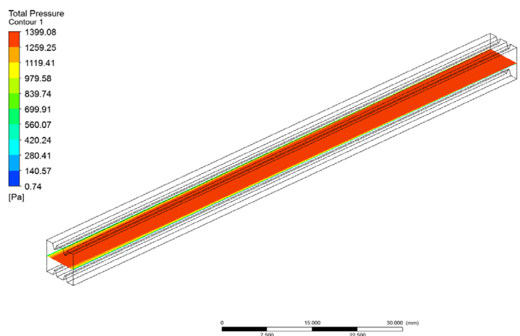

b)

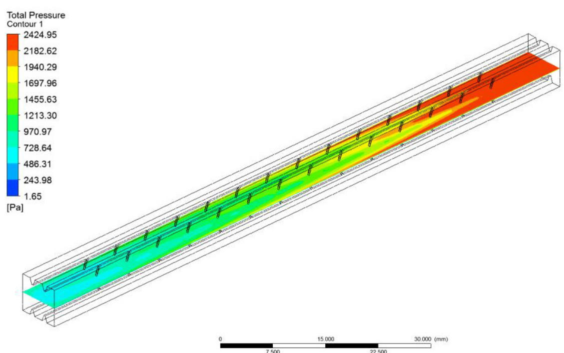

c)

Figure 22. Pressure losses in single channel with and without ribs (a), total pressure in the smooth (b) and ribbed channel (c)

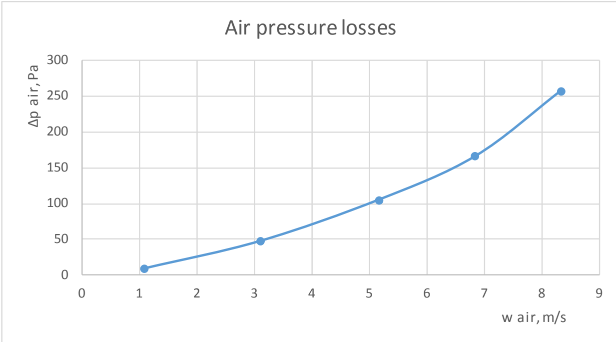

a)

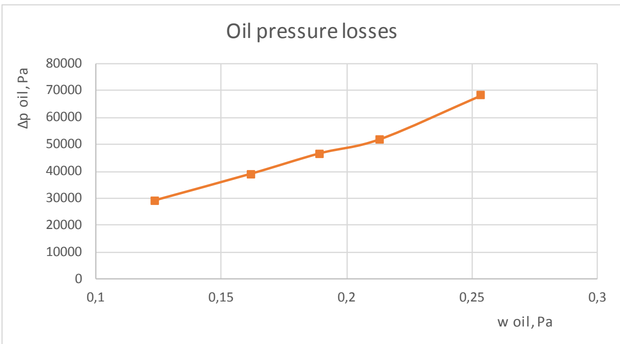

b)

Figure 21. Air and oil pressure losses in dependency on air and oil flow velocity (determined numerically)

Table 9. Oil pressure losses in dependence on oil mass flow rate of a single channel

Parameter	Value							
One channel mass flow rate $G_{oil\ 1\ ch}$, kg/s	0,001	0,003	0,007	0,01	0,015	0,02	0,025	0,03
Oil losses with ribs $\Delta p_{rib\ ch}$, Pa	0,78	6,10	29	57	124	214	323	469
Oil losses without ribs $\Delta p_{sm\ ch}$, Pa	0,35	2,3	10	19	39	64	93	133
$\Delta p_{rib\ ch}/\Delta p_{sm\ ch}$	2,2286	2,6522	2,9000	3,0000	3,1795	3,3438	3,4731	3,5263

4. Discussion

The following is the thermal and hydraulic parameters analysis of the cooling section obtained by the experimental and numerical methods.

The experimental results analysis was done at fixed mass flow rates of both heat carriers based on exploitation conditions G_{oil} = 0.31±0.1 kg/s and G_{air} = 0.36±0.1 kg/s respectively. In view of tube parameters changing, velocities (therefore and Reynolds numbers) and heat transfer coefficients are changed, as well, both inside and outside (Figure 7). It is necessary to point at the fact that the flat-finned tube specific gravity changes in the range from 0.802 to 1.025 kg/m (Table 4) at the fin height change from 4 to 8.5 mm (Table 3) according to the sample number.

The maximum thermal efficiency fixed for sample 5 having 8 mm fin height and 2.5 mm fin pitch in combination with 67.5 mm tube width and 8.3 mm tube height with eight inner channels (Table 4, Figure 6). This sample has the largest heat transfer area in comparison with other samples due to thick finning and greater tube width.

It should be noted that sample 1 having similar fin dimensions (and 8.5 fin height) but smaller tube width than sample 5 (therefore, smaller heat transfer area), provides almost the same thermal power transfer. It is explained by the fixed oil flow rate during the experiment. The fact is that sample 1 has smaller oil cross section area than sample 5 has; therefore, the oil velocity in sample 1 is higher than in sample 5. As a result, the heat transfer coefficient of sample 1 is higher and the thermal resistance coefficient of sample 1 is less than the same parameters of sample 5. Thus, sample 1 has the design, which can lower weight and dimensional characteristics of an air-to-oil heat exchanger at fixed parameters of an oil pump unit and fun installation. Meanwhile, samples 2 - 4 having similar small cross-section areas but fin pitches in the range of 2 to 3.75 mm and fin heights of 4 to 6.5 mm, show the worst results of thermal efficiency.

Sample 7 has the lowest compactness factor and the thermal efficiency value, which is comparable to sample 3. Such a low value of thermal power caused by a big fin pitch and small fin height of the sample 7 design. Therefore, the main reason for low thermal efficiency of sample 7 is poorly developed heat exchange surface.

Sample 6 has the lowest thermal efficiency despite the similar design to sample 5. The most possible reason of this phenomenon is the highest total thermal resistance to heat transfer caused by the nonoptimal sample design. However, in this case, a random error in the acquisition and processing of experimental data is possible, as well.

Thermal power grows steadily with a stable growth of Reynolds number (Figure 7). An increase in Reynolds numbers leads to an increase of turbulence; therefore, the turbulence intensifies the heat exchange process, thereby causing an increase in heat transfer coefficients. Thus, the Reynolds numbers growth has a positive effect on the heat transfer process but a negative effect on the heat exchanger hydraulic characteristics, in particular on pressure losses, so evaluating of power costs for pumping the heat carrier is another significant aspect in heat exchanger design process.

The mutual influence of both factors (thermal efficiency and pressure losses) on the heat exchanger design can be evaluated with Kirpichev and Antufiev energy efficiency criterions. Usually, high thermal performance is possible to achieve at the simultaneous increase of pressure losses, consequently increasing power costs for pumping the energy carrier.

The highest value of Kirpichev criterion (Figure 8) corresponds to optimal heat exchanger dimensions, which provide the most effective heat transfer at the minimum of power costs for pumping the heat carrier. Samples 1-3 have the highest air side energy efficiency criterion (N_{air}), simultaneously, these samples show worsening Kirpichev criterion concerning the oil side pumping power (N_{oil}) because of the flow area decrease and oil velocity increase in inner channels. Sample 5 has the maximum total Kirpichev criterion ($N_{air} + N_{oil}$) value.

The chart represented in Figure 9 shows that sample 3 has the highest values of Antufiev criterion. Thus, sample 3 has the most profitable indicators of the heat exchanger aerodynamic and hydraulic perfection due to low values of pressure loss, both air and oil sides. However, in comparison with samples 3 and 5, thermal efficiency of sample 3 is much less because of smaller heat transfer area.

Based on the foregoing, it is possible conclude that the most effective thermodynamic performance has sample 5, but the optimal combination for all the parameters can be considered sample 1.

As it was said before, the main goal of the numerical investigation is obtaining an adequate model of a single cooling section for the subsequent creation of the whole oil cooler model. The cooling section numerical investigation is conducted for different boundary conditions in the oil side and air side parameters range. Figure 22 shows some results of the experimental and numerical data comparison done for samples 1-4 (Table 4) with respect to the main thermodynamic parameters. It can be seen from the graphs in Figure 23 that for the case of six-channel finned tube samples 1-4, good comparability of the natural and numerical experiment results is observed.

The curve trends of the experimental (Figure 6) and numerical (Figure 21b) hydraulic resistance graphs coincide, confirming the adequacy of the numerical model.

The coincidence of experimental and numerical data, confirming the adequacy of the cooling section model, allows to get the first reference point to continue further research with a full-sized oil cooler as part of an automatic air-to-oil heat exchanger in a single container. In this case, a particular interest is the mutual influence of the heat exchange sections to the oil heat exchanger operation. For instance, for the case of a two-row heat exchanger, the following air flow pattern is possible (Figure 24).

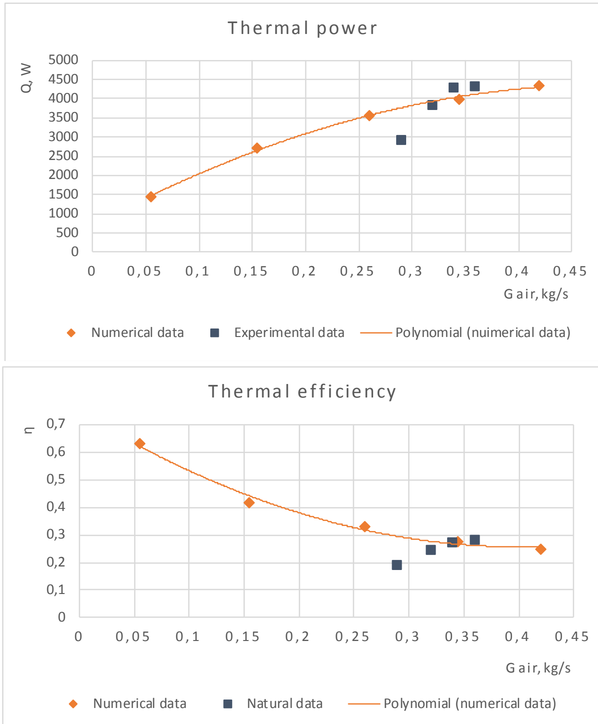

Figure 23. Comparison of numerical and experimental data (thermal parameters)

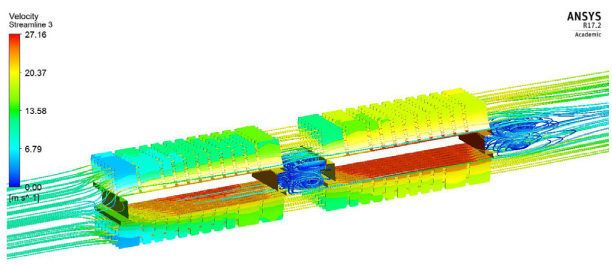

Figure 24. The double-row heat exchanger flow structure of the air domain

5. Conclusions

The effective project solution of a modern air-to-oil heat exchanger directly depends on an optimal combination of thermal efficiency, geometry and weight characteristics of an exchanger basic element.

The usage of the cooling section with increased thermal efficiency (sample 5) will allow to enhance amount of heat removed by the exchanger insignificantly but the usage the cooling section with optimal dimensional characteristics (sample 3) will allow to get an oil cooler with lower specific quality of metal per structure with almost the same efficiency. In addition, the practical application of this section (sample 3) will lead to lower energy costs for pumping, which is important when working as part of an entire lubrication system. Therefore, the design of sample 3 is the most preferable variant for use and installation into the full-sized oil cooler.

As a recommendation, from the aerodynamic point of view, the ends of flat pipes should be produced rounded to reduce air pressure losses. According to studies [11,12] this design allow to increase the thermal hydraulic efficiency in comparison with round and oval pipes having a different layout of ribs.

Despite the good convergence of the natural and numerical investigations results, it should be noted that in this study, heat and mass transfer processes of insulated flat finned tubes were investigated. At the same time, it is necessary to consider that the isolated experimental conditions of the single cooling section test do not correspond to the actual operating conditions as part of a full-sized oil cooler. The mutual influence of the tubes, the effect of collecting and distributing collectors, should be considered as part of a separate study of a fully assembled oil cooler. Additionally, when installing an oil cooler into an automatic air-to-oil heat exchanger, the influence of the walls, internal elements of a container and the influence of external blinds should be taken into account, as well.

For taking into account all of the above factors affecting the heat transfer process, it is important to set the boundary conditions as correctly as possible. However, even in the case of correctly specified boundary conditions, a directed natural experiment is required to confirm the adequacy of the developed model for both the oil cooler and the cooling apparatus in the container.

References

[1] Chichindaev, A.V., 2009. Teplomassoobmen vlazhnogo vozdukha v kompaktnikh plastinchato-rebristikh teploobmennikakh, Novosibirsk, NGTU. pp. 298. (in Russian).

[2] Bessonny, A.N., Dreicer, G.A., Kuntish, V.B., 1996. Osnovi rascheta i proektirovaniya teploobmennikov vozdushnogo okhlazhdeniya [Calculation and design foundations of air cooled heat exchangers], St.Petersburg, Nedra Publ. pp. 512. (in Russian).

[3] Pismennii, E.N., 2004. Teploobmen i aerodinamika paketov poperechno-orebrennikh trub, Alterpres Publ. pp. 243. (in Russian).

[4] Popov, I.A., Makhyanov, Kh.M., Gureev, V.M., 2009. Fizicheskie osnovi i promishlennoe primenenie intensifikacii teploobmena: Intensifikaciya teploobmena: monografia, Kazan, Center innovacionnikh tekhnologii. pp. 560. (in Russian).

[5] Deulin, K.N., et al., 2008. Teploobmenny element [The heat exchanging element]. Patent RF, no. RD0039306.

[6] Lemouedda, A., Schmid, A., Franz, E., Breuer, M., Delgado, A., 2011. Numerical investigations for the optimization of serrated finned-tube heat exchangers. Applied Thermal Engineering. 31(8-9), 1393-1401. DOI: https://doi.org/10.1016/j.applthermaleng.2010.12.035.

[7] Popov, I.A., Makhyanov, Kh.M., Gureev, V.M., 2009. Phisicheskie osnovi i promishlennoe primenenie intensifikacii teploobmena [Physical foundations and industrial application of heat exchange intensification], Kazan, Center innovacionnikh tekhnologii. pp. 560. (in Russian).

[8] Khabibullin, I.I., Nizamutdinoiv, R.M., Kadyrov, R.G., Nikolaenko, I.V., Gureev, M.V., Tiunov, S.V., 2019. Numerical modelling of heat exchange processes in the oil air cooling device. Gazovaya promishlennost. 2, 84-90. (in Russian).

[9] Bazhan, P.I., Kanevets, G.E., Seliverstov, V.M., 1989. Spravochnik po teploobmennim apparatam, Moskva, Mashinostroenie Publ. pp. 368. (in Russian).

[10] Antufiev, V.I., 1966. Effectivnoct razlichnikh form konvektivnikh poverkhnostei nagreva. Mockva, Energiya Publ. pp. 183. (in Russian).

[11] Pismennii, E.N., Demchenko, V.G., Terekh, A.M., 2010. Ecomomaizer-utilizator iz plosko-ovalnikh trub s nepolnim orebreniem. Vostochno-evropeiskii zhurnal peredovikh tekhnologii. no 3/1(45). pp. 15-19 (in Russian).

[12] Judin, V.F., Fedorovich, E.D., 1991. Teploobmen puchkov orebrennikh trub ovalnogo profilya. Teplomassoobmen. MMF-92. Konvektivnii teplomassoobmen. Vol. 1, part 1, Minsk, ANK ITMO ANB. pp. 58-61 (in Russian).

SCIENTIFIC
Publishing Limited

Tel.: +44 122 360 3549
Email: contact@ukscip.com
Website: http://ojs.ukscip.com

2754-5652
01
9 772754 565227